UNIVERSIDAD DE GRANADA
DEPARTAMENTO DE FÍSICA ATÓMICA, MOLECULAR Y NUCLEAR

Estudio de la fluorescencia de un ion de $^{40}Ca^{+}$ en una trampa magnética de 7 T

Manuel Jesús Gutiérrez Torres

Director: Daniel Rodríguez Rubiales

Master Thesis

July 2016

UNIVERSIDAD DE GRANADA
DEPARTAMENTO DE FÍSICA ATÓMICA, MOLECULAR Y NUCLEAR

Title: "Estudio de la fluorescencia de un ion de $^{40}Ca^{+}$ en una trampa magnética de 7 T"

Author: Manuel Jesús Gutiérrez Torres

Center: Facultad de Ciencias, Universidad de Granada

Department: Dpto. de Física Atómica, Molecular y Nuclear

Director: Daniel Rodríguez Rubiales

EL DIRECTOR DE TESIS,

Fdo. D. DANIEL RODRÍGUEZ RUBIALES

Acknowledgements

First of all, I would like to thank my Master Thesis director, Daniel, for the great opportunity he provided me now almost 2 years ago, for the patience he has shown during that time, and for his support and dedication. He is a living example of what passion for research should look like.

The TRAPSENSOR team is everything one could ask for and more. Thanks to Fran for the company and help, and to Jaime for his positive attitude, considerate opinions and selfless help. A special mention goes to (Dr!) Juanma, to whom I offer my most sincere gratitude. He helped me a great deal with all the aspects of this work. I hope you have the best of luck in this new stage of your life. I also wanted to thank Prof. Günter Werth for his help during his visit and for making me see there is physics even in the most rutinary lab task.

If someone must appear in this acknowledgements, it is Cristina. She has listened to my explanations about ion trapping and laser cooling so many times that she should get college credits for it. Thank you for everything. Last, but not least, I want to thank my parents and sister. They give the kind of support that only comes from family.

Abstract

In this work, the latest developments towards Doppler cooling in a 7 T magnetic field in the framework of the TRAPSENSOR project are presented. First, a brief introduction to mass measurements in Penning traps and the goal of the TRAPSENSOR project are introduced. Then, the dynamics of ions stored in Penning traps are explained, and Doppler cooling is introduced for the particular case of $^{40}Ca^{+}$ ions in a 7 T magnetic field. The experimental setup is also described underlining the modifications carried out in this work and resulting in the first time-of-flight ion-cyclotron resonance performed with an open-ring Penning trap. These modifications also pave the way for Doppler cooling. Finally, the principle of using a laser-cooled ion as detector has been discussed from measurements carried out with two open-ring ion traps.

Keywords: ion, trap, doppler, cooling, resonance

Resumen

En este trabajo se recogen los últimos avances hacia el enfriamiento Doppler en un campo magnético de 7 T en el marco del proyecto TRAPSENSOR. En primer lugar se da una breve introducción de las medidas de masa en trampas Penning y el objetivo del proyecto. A continuación, la dinámica de iones atrapados en trampas Penning es explicada y se introduce la técnica de Doppler cooling, prestando atención a los efectos del campo magnético. El siguiente paso es una descripción del setup experimental, junto con las modificaciones implementadas de cara al enfriamiento Doppler y la optimización de varias de sus partes, así como la primera resonancia de tiempo de vuelo obtenida en una trampa de anillos. Por último, se discuten las ventajas que aporta el uso de un ion enfriado por láser como detector, comparando medidas en dos trampas de similar geometría.

Palabras clave: ion, trampa, enfriamiento, doppler, resonancia

Contents

List of Figures

Chapter 1

Introduction

Ion traps are very powerful instruments for fundamental research, since a charged particle can be confined in a small volume in phase-space, allowing for the realization of very accurate experiments. Many branches in physics profit from the performance of ion traps; two remarkable examples, away from each other, are quantum information [1, 2, 3], and high-precision measurements of ground-state properties (e.g. masses) of isolated particles [4, 5, 6, 7].

The most accurate determination of the atomic mass is provided with an ion trap (Penning trap specifically) and since the mass yields directly the binding energy in a nuclear system, mass measurements on exotic ions have been used to test nuclear models in extreme conditions [8], to provide useful data for stellar nucleosynthesis [9], or to test the Standard Model [10]. The masses of stable or long-lived particles can be measured with a relative mass uncertainty ($\delta m/m$) in the order of 10^{-11}, allowing the use these values to test theories and expressions such as the Einstein's relationship $E = mc^2$ [11], and to determine fundamental constants such as α [12], among other things.

There are several techniques to perform mass measurements using Penning traps. The Time-Of-Flight Ion-Cyclotron-Resonance (TOF-ICR) technique, which will be described in detail in this Master Thesis [13], is a destructive technique that needs several tens of ions and allows reaching relative mass uncertainties in the order of 10^{-9}. This is widely used with ions produced at accelerators, and although many relevant results have been obtained with it, it is limited by the ion-production rate because of the statistics needed for the measurement. The lowest production rate of an ion reached so far in a Penning-trap experiment is $0.5\,\mathrm{h}^{-1}$ [14]. A more recent technique, known as Phase-Imaging Ion-Cyclotron-Resonance (PI-ICR), makes use of a position-sensitive detector [15] to improve the precision by a factor of 40 and reduces the time required to make a measurement in a factor of 25 with respect to the TOF-ICR [16]. This technique has not been applied yet

to exotic ions and would need around $10-20$ ions for the measurement.

The technique in use up to date for stable particles is the so-called Induced-Image-Current (IIC) technique, where the ion's characteristic frequencies and thus its mass, are determined from the electric current the ion induces in the trap's electrodes [17]. This technique allows reaching the 10^{-11} level, but it has only been demonstrated for ions with low or medium mass-to-charge ratios.

The TRAPSENSOR project at the University of Granada aims at implementing a new technique for mass measurements [18] to overcome the present limitations regarding sensitivity (TOF-ICR and PI-ICR), allowing for single ion detection, and universality (IIC), to make practicable any mass-to-charge ratio. It is based on a previous proposal by Heinzen and Wineland [19]. A trapped and laser-cooled $^{40}Ca^{+}$ ion will be used as mass detector or *sensor ion*. The ion of interest, whose mass has to be measured, is trapped in an identical trap, oscillating with the same axial frequency, and inducing charge in a common electrode, thus transferring energy resonantly to the sensor ion. The ion of interest is previously probed with an external time-varying field at a frequency equal to one of its mass-dependant frequencies, so that its motional energy increases. The energy transferred to the laser-cooled (sensor) ion will be observed in the optical regime using its fluorescence photons.

The work presented in this Master Thesis has been devoted to study and develop the instrumentation needed to perform Doppler cooling on the $^{40}Ca^{+}$ ion in the 7 T magnetic field of the Penning trap and to study the feasibility of the proposed method in this kind of trap, extrapolating from laser-cooling measurements performed in a non-magnetic trap with similar geometry. The Thesis is organized as follows: A theoretical introduction to Penning traps and laser cooling will be given in Ch. 2, including the essential aspects under study in this work, i.e., J-mixing, Zeeman splitting, directionality and polarization, particularly focussed on the $^{40}Ca^{+}$ ion. In Ch. 3, the experimental setup is presented, both the Penning-traps beamline and the lasers and optical setup. After building the open-ring Penning trap with all the elements needed to perform laser cooling in the 7 T magnetic field, $^{40}Ca^{+}$ has been probed with external radiofrequency fields. From the measurements carried out so far, some conclusions can be extracted about this novel laser-based mass-measurement method.

Chapter 2

Methodology

In this chapter, the classical dynamics of an ion in a Penning trap will be explained, along with several techniques used to manipulate the ion's motion. The Doppler cooling technique will be introduced, focussing on the cooling in a 7 T Penning trap and the important issues like J-mixing, Zeeman splitting, and the discussion about the optimal directions and polarizations for the 12 laser beams needed for the sensor ion.

2.1 Penning traps

In an ion trap, a restoring force for the charged particle is required, and the simplest and most convenient way to obtain this force is from a harmonic oscillator:

$$V(x,y,z) = \frac{1}{2}\left(\alpha x^2 + \beta y^2 + \gamma z^2\right) \ , \tag{2.1}$$

where α, β and γ are constants.

In absence of charges, this potential must verify Laplace's equation; thus,

$$\nabla^2 V(x,y,z) = \alpha + \beta + \gamma = 0 \ , \tag{2.2}$$

which implies that at least, one of the constants must be negative, and thus the potential has to be repulsive in at least one direction. Therefore trapping is not possible with only electrostatic potentials.

There are two common ways to circumvent this, the first one is by applying an AC potential that results in an average 'pseudopotential', attractive in all directions, and the second one based on the combination of an electrostatic field with cylindrical symmetry, that is, $\gamma = -2\alpha = -2\beta > 0$, and a magnetic field $\vec{B} = B\,\hat{z}$,

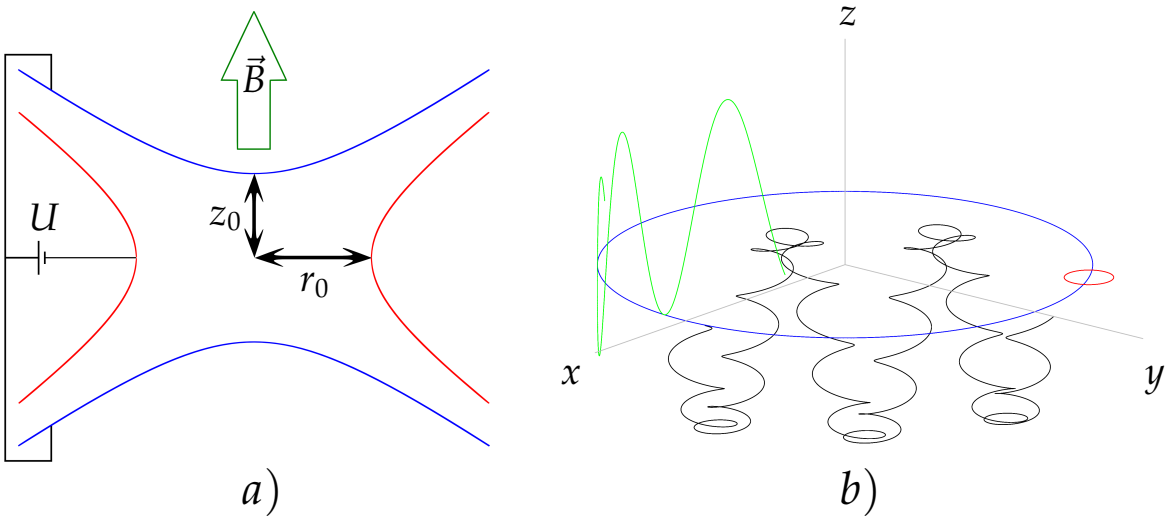

Figure 2.1: Left: sketch showing a longitudinal cut of a hyperbolic Penning trap. The ring and endcap electrodes are depicted in red and blue, respectively. The trap has cylindrical symmetry along the axis defined by the magnetic field (thick green arrow). Right: ion's motion in a Penning trap (black-solid line). The ion's motion is the superposition of the three individual motions: the axial motion is shown in green, the magnetron motion in blue, and the reduced-cyclotron motion in red.

strong enough to counteract the repulsive effect of the electrostatic potential in the radial direction. The devices using AC potentials are known as Paul or RF traps, while the others are known as Penning traps.

2.1.1 Ion motion in a Penning trap

The potential in a Penning trap such as the one shown in Fig. 2.1a can be written as

$$V(x,y,z) = \frac{U}{2z_0^2 + r_0^2}\left(2z^2 - x^2 - y^2\right) = \frac{U}{4d_0^2}\left(2z^2 - x^2 - y^2\right), \tag{2.3}$$

where $d_0 = \frac{1}{2}\sqrt{2z_0^2 + d_0^2}$. The classical equations of motion of an ion in a Penning trap read:

$$\vec{F} = q\left(\vec{E} + \vec{v}\times\vec{B}\right) = q\left(-\nabla V + \vec{v}\times B\,\hat{z}\right) \Rightarrow \begin{cases} \ddot{x} = \frac{qU}{2md_0^2}x + \frac{qB}{m}\dot{y} = \frac{1}{2}\omega_z^2 x + \omega_c\dot{y} \\ \ddot{y} = \frac{qU}{2md_0^2}y - \frac{qB}{m}\dot{x} = \frac{1}{2}\omega_z^2 y - \omega_c\dot{x} \\ \ddot{z} = -\frac{qU}{md_0^2}z = -\omega_z^2 z \end{cases}, \tag{2.4}$$

where $\omega_c = qB/m$ is the ion's cyclotron frequency.

The z equation is that of a harmonic oscillator, with frequency

$$\nu_z = \frac{\omega_z}{2\pi} = \frac{1}{2\pi}\sqrt{\frac{qU}{md_0^2}} \ . \tag{2.5}$$

The equations in x and y are coupled and to treat them, the variable $u = x + iy$ is defined. The resulting equation, $\ddot{u} = \omega_z^2 u/2 - i\omega_c \dot{u}$ can be solved; the resulting radial motion is a superposition of two circular motions with frequencies

$$\omega_\pm = \left(\frac{\omega_c}{2} \pm \sqrt{\frac{\omega_c^2}{4} - \frac{\omega_z^2}{2}}\right) \ . \tag{2.6}$$

ω_+ is the so-called 'reduced cyclotron frequency', and ω_- is the 'magnetron frequency'. The motion is purely oscillatory (and therefore bounded) if $\omega_\pm$ are real:

$$\omega_\pm = \frac{\omega_c}{2} \pm \sqrt{\frac{\omega_c^2}{4} - \frac{\omega_z^2}{2}} \in \mathbb{R} \Rightarrow \frac{\omega_c^2}{4} - \frac{\omega_z^2}{2} > 0 \Rightarrow \omega_c > \sqrt{2}\omega_z \, . \tag{2.7}$$

The ion's trajectory is shown in Fig. 2.1b.

It is worth mentioning that the magnetron motion is mass independent, i.e,

$$\omega_- \simeq \frac{U}{2Bd_0^2} \neq f(m) \tag{2.8}$$

up to the fourth order in ω_z/ω_c. The independency between ω_- and the mass of the trapped ion is used in mass-selective ion cooling [20, 21, 22]. Important relationships between the frequencies are

$$\omega_c = \omega_+ + \omega_- \ , \tag{2.9}$$

for an ideal Penning trap,

$$\omega_c^2 = \omega_+^2 + \omega_z^2 + \omega_-^2 \ , \tag{2.10}$$

known as 'invariance theorem', which holds for *real* Penning traps, i.e., traps with deviations from the quadrupole electric field or because of magnetic field misalignments [23], and

$$\omega_c \sim \omega_+ \gg \omega_z \gg \omega_- \ , \tag{2.11}$$

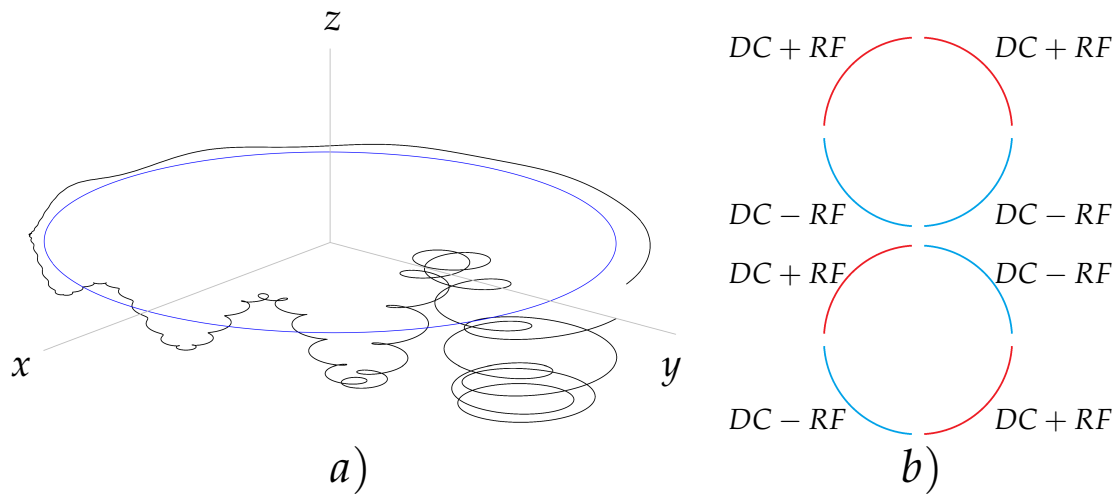

Figure 2.2: Left: evolution of the ion's trajectory in a Penning trap due to collisions with buffer-gas atoms (black-solid line). The blue line is the initial magnetron motion, shown as a reference. Right: configuration of the potentials applied to a four-fold segmented ring electrode for dipolar excitation (top) and quadrupolar excitation (bottom). The RF (oscillatory) term on the blue electrodes has a 180° shift with respect to that of the red ones, as indicated by the minus sign.

which is a consequence of the usual experimental conditions.

2.1.2 Motion manipulation

In a Penning trap the ion's motion can be manipulated by applying external time-varying fields with different polarities and directions, in resonance with any motional frequency of the ion, or resulting from linear combinations. In addition, one might use these fields in combination with resistive forces or magnetic-field gradients.

The techniques utilized in this work will make use of the following physical effects:

- Buffer gas: when gas is injected into the trap, the ions will collide with the gas's atoms, and this originates an average force given by $\vec{F} = -\delta m\vec{v}$ [13], which decreases the energy, and thus the amplitude, of the reduced-cyclotron and axial motions. On the other hand, the magnetron amplitude increases when the energy is reduced (see Fig. 2.2a), due to the unstable nature of the magnetron's motion.

- Time-varying dipole and quadrupole fields in the radial direction: the required geometry and segmentation is shown in Fig. 2.2b. A dipole field

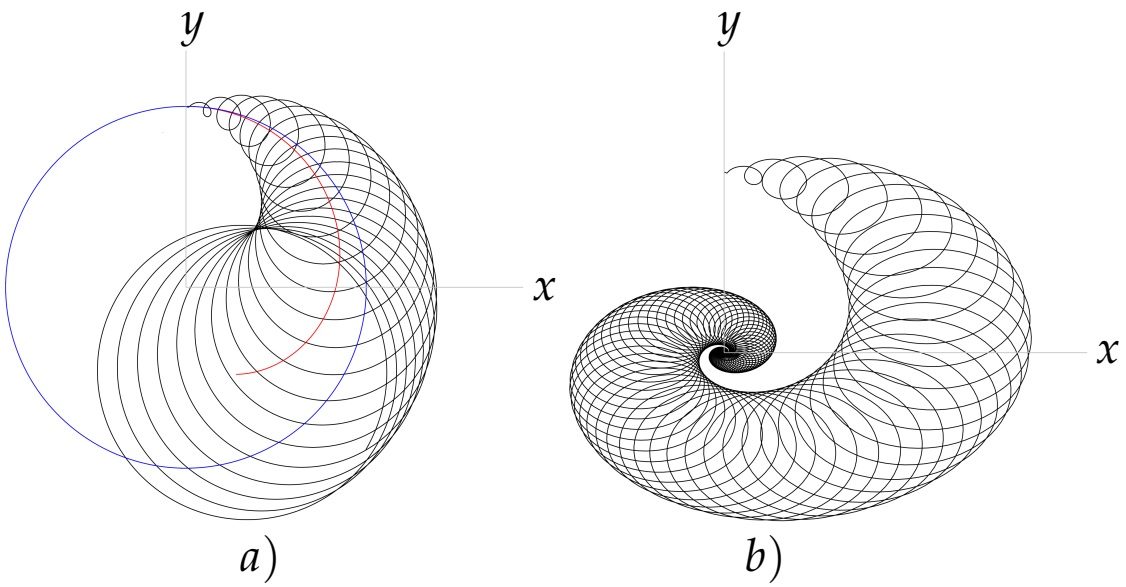

Figure 2.3: Left: evolution of the ion's trajectory when applying a quadrupole field oscillating at ν_c (black-solid line). The initial motion (only magnetron, blue line) is gradually converted to reduced-cyclotron. The red line shows the evolution of the magnetron amplitude. Right: evolution of the ion's trajectory when applying the same quadrupole field in a trap filled with gas. The amplitude of the magnetron motion decreases because of the conversion, while reduced-cyclotron amplitude decreases because of collisions with the buffer-gas atoms. The final effect is centering the ion, provided the damping, and the amplitude and duration of the quadrupole field are properly set.

oscillating at a characteristic frequency of the ion's motion originates an increase of the amplitude of that motion. If the field is quadrupolar, oscillating at the cyclotron frequency $\omega_c = \omega_+ + \omega_-$, the effect is a periodic energy transfer between the two radial motions, similar to Rabi oscillations in a two-level system [13] (see Fig. 2.3a).

- Magnetic field gradient: when an ion is extracted from a magnetic field, the magnetic field gradient causes a force due to the ion's dipolar magnetic moment [13]:

$$\begin{cases} \vec{F} = -\nabla\left(\vec{\mu}\cdot\vec{B}\right) \\ \vec{\mu} = \frac{E_r}{B}\hat{z} \end{cases} \quad \Rightarrow F_z = -\mu_z \frac{\partial B_z}{\partial z} \propto E_r \tag{2.12}$$

Following this equation, higher radial energies will result in a lower time of flight from the trap center to the detector.

The two techniques of relevance for this work are:

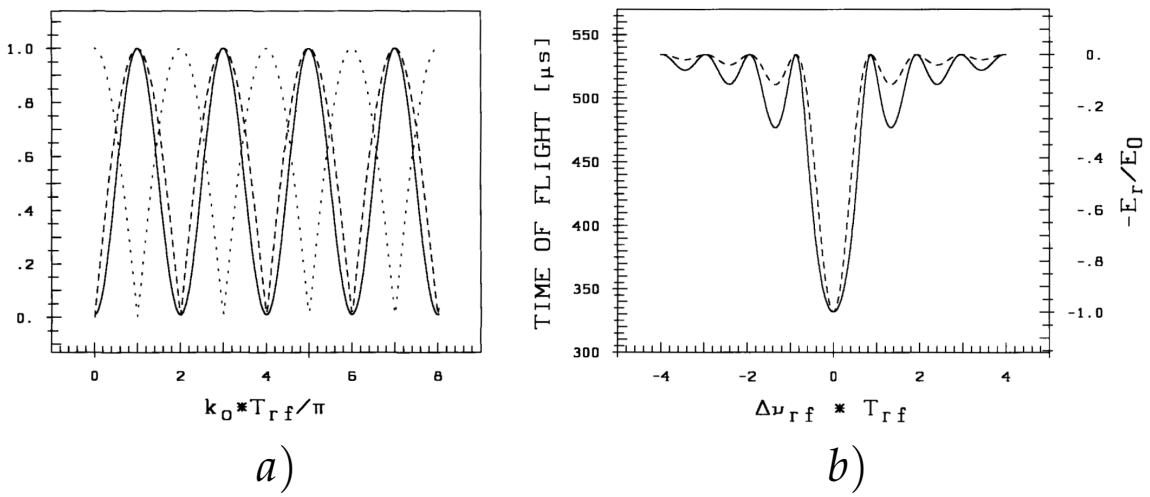

Figure 2.4: Extracted from [13]. Left: conversion of the radial motions as a function of the amplitude (proportional to k_0) and the duration T_{RF} of the quadrupolar field. The solid line represents the evolution of the radial kinetic energy normalized to the maximum E_r/E_0. The dashed and dotted lines are ρ_+/ρ_0 and ρ_-/ρ_0, which are the reduced-cyclotron and magnetron amplitudes normalized to the maximum amplitude in the radial plane ρ_0. Right: theoretical line shape of a cyclotron resonance. The dashed line represents the radial kinetic energy while the solid one is the resulting time-of-flight if the ins are extracted towards a micro-channel plate detector. $\Delta\nu_{RF} = \nu_{RF} - \nu_c$.

- The buffer-gas cooling technique [20]: a dipolar field oscillating at ω_-, followed by a quadrupolar field oscillating at ω_c are applied in a gas-filled trap. The effect is shown in Fig. 2.2b). This has been thoroughly described in previous works [21, 22]. This technique has a resolving power that allows isobaric separation.

- The Ion-Cyclotron-Resonance Time-Of-Flight (TOF-ICR) technique: a dipolar field oscillating at ω_-, followed by a quadrupolar field oscillating at ω_c are applied, in this case, in absence of gas. The application of these fields in this order results into a large magnetron orbit, followed by the conversion from magnetron to reduced-cyclotron. Once this is accomplished, the ions are extracted from the trap. Scanning the frequency of the quadrupolar field around $\omega_c = qB/m$ results in the time-of-flight spectrum shown in Fig. 2.4b).

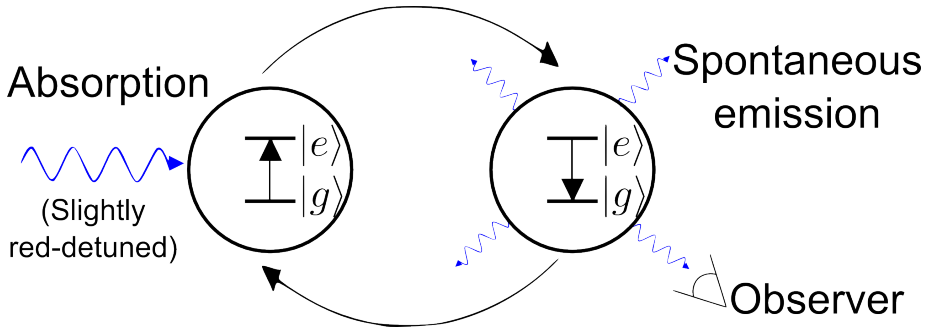

Figure 2.5: Doppler cooling cycle. Since the laser is red-detuned, the photon absorptions typically take place when the particle moves opposite to the photons of the laser beam, thus reducing the particle's momentum. The emitted photons are collected and used to monitor the process.

2.2 Doppler cooling in a 7 T magnetic field

2.2.1 General description and Doppler limit

The Doppler cooling technique was simultaneously proposed in 1975 by T.W. Hänsch and A.L. Schawlow for atoms [24] and by D.J. Wineland and H. Dehmelt [25] for ions, and realized experimentally for the first time, three years later by W. Neuhauser *et al* [26] and by D.J. Wineland *et al* [27]. With this mechanism it is possible to reduce the kinetic energy of the trapped ion down to miliKelvin.

Doppler cooling is carried out using an electric dipole transition in the electronic structure of an ion, i.e., the transition from the electronic ground state $|g\rangle$ to an excited state $|e\rangle$, as depicted in Fig. 2.5. If a laser is tuned to a frequency ω_L slightly below the one of the transition between $|g\rangle$ and $|e\rangle$, represented by ω_0, i.e., $\omega_L = \omega_0 + \Delta$ and $\omega_0 \gg |\Delta|$, with $\Delta < 0$, a photon will be absorbed when the particle this moves in the opposite direction to the photon, and then will be reemitted via spontaneous decay. If the process is repeated many times, the recoil due to the emitted photons will average to zero, whereas the absorption contribution will not. The absorptions will preferentially transfer momentum in the opposite direction to the particle's motion. This results in a reduction of momentum and kinetic energy.

This intuitive description of Doppler cooling is supported by a rigorous theoretical treatment; it is possible to prove that the variation of kinetic energy is given by [28]

$$\dot{E}_c = \langle F_a v \rangle = F_0 \kappa \left\langle v^2 \right\rangle , \tag{2.13}$$

where κ has the same sign as the detuning of the laser, $\Delta = \omega_L - \omega_0$, and F_0 is

the averaged radiation pressure. Thus, there is cooling ($\dot{E}_c < 0$) if $\Delta < 0$, which corresponds to a red-detuned laser.

Some heating of the ion occurs due to the reemission of the photons. The equilibrium between cooling and heating dictates the equilibrium temperature [28],

$$\dot{E}_c + \dot{E}_h = 0 \Rightarrow T_{min} = \frac{\hbar\Gamma\sqrt{1+s}}{4k_B}(1+\xi) \ , \tag{2.14}$$

where k_B is the Boltzmann's constant, ξ is a geometrical factor which takes into account the spontaneous emission pattern of the particle and s is the saturation parameter, $s = I/I_0$, where I is the laser's intensity and I_0 the so-called saturation intensity.

This technique can be applied to cool[1] the axial and reduced-cyclotron motions. The magnetron motion, however, is heated, because the amplitude increases when magnetron energy is extracted. Cooling of this motion can be achieved in two ways [29]:

- Using a laser beam with non-uniform intensity profile: if the laser is offset from the trap center, pointing in the same direction as the magnetron motion, an intensity gradient along the radial direction appears (see Fig. 2.6), and more photons will be absorbed in the region where the particle moves away from the laser beam, increasing the magnetron motional energy, and therefore decreasing the amplitude. The reduced-cyclotron motion is cooled normally, as the whole reduced cyclotron orbit is within the laser beam. This method has a severe disadvantage: the laser offset and its spot size limit the minimum magnetron orbit that can be achieved.

- Coupling between the radial motions: coupling the magnetron and reduced-cyclotron motion using a oscillating quadrupole field in the presence of the laser beam has a similar effect as the combination of the same quadrupole excitation and buffer gas (see Fig. 2.3b). The magnetron amplitude is reduced because of the conversion, while the reduced-cyclotron amplitude is reduced because of the Doppler cooling.

Axial and radial motions can also be coupled using a quadrupole field, albeit with a different geometry (see e.g. [21]), so the axial motion can be also cooled without an axial laser beam.

Doppler cooling of $^{40}Ca^+$ (the ion of interest in this work) requires more than one laser beam. This is because its electronic structure, accessible with commercial

[1] In this context, cooling a particular motion means reducing its amplitude.

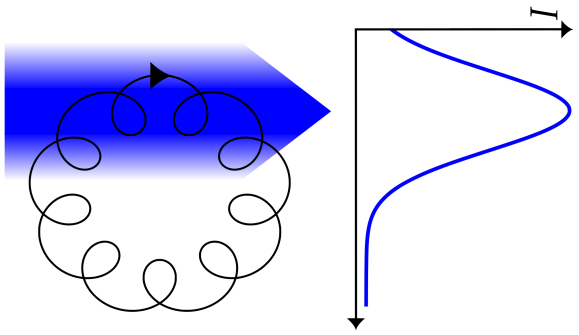

Figure 2.6: A laser beam offset from the center results in an intensity gradient along the radial direction. If the intensity is bigger where the ion moves away from the laser, the magnetron motion will be cooled.

diode lasers, has two metastable levels between the ground ($S_{1/2}$) and excited ($P_{1/2}$) states, $D_{3/2}$ and $D_{5/2}$ (see Fig. 2.7). If these levels are populated by spontaneous decay, the cooling cycle is interrupted; thus, optical pumping is required to depopulate the levels and resume the cooling process. Although the decay $P_{1/2} \rightarrow D_{5/2}$ is strongly forbidden, it can take place in the presence of magnetic fields [30] (see Sec. 2.2.2).

2.2.2 J-mixing and Zeeman splitting

The presence of a magnetic field causes a splitting of the energy levels of an atomic system and a mixing of the states with different J number. Both effects are of importance for Doppler cooling in Penning traps, and will be addressed in this section.

The electric-dipole moment matrix element $M = \left\langle D_{5/2} \left| \vec{d} \cdot \vec{E} \right| P_{1/2} \right\rangle$ is zero. However, a magnetic field will cause a J-mixing effect [30]. The matrix element is then

$$M' = \left\langle D'_{5/2} \left| \vec{d} \cdot \vec{E} \right| P'_{1/2} \right\rangle = \left(\langle D_{5/2}| + \epsilon_D \langle D_{3/2}| \right) \vec{d} \cdot \vec{E} \left(|P_{1/2}\rangle + \epsilon_P |P_{3/2}\rangle \right) \simeq$$
$$\simeq \epsilon_D \left\langle D_{3/2} \left| \vec{d} \cdot \vec{E} \right| P_{1/2} \right\rangle + \epsilon_P \left\langle D_{5/2} \left| \vec{d} \cdot \vec{E} \right| P_{3/2} \right\rangle \quad , \quad (2.15)$$

where a term in $\epsilon_D \epsilon_P$ has been neglected. The coefficients ϵ_D and ϵ_P are given by [30]

$$\epsilon_D = \frac{\left\langle D_{3/2} \left| \vec{\mu} \cdot \vec{B} \right| D_{5/2} \right\rangle}{E_{D_{5/2}} - E_{D_{3/2}}} \qquad \epsilon_P = \frac{\left\langle P_{3/2} \left| \vec{\mu} \cdot \vec{B} \right| P_{1/2} \right\rangle}{E_{P_{1/2}} - E_{P_{1/2}}} \quad (2.16)$$

from first-order perturbation theory. The two matrix elements in Eq. 2.15 are

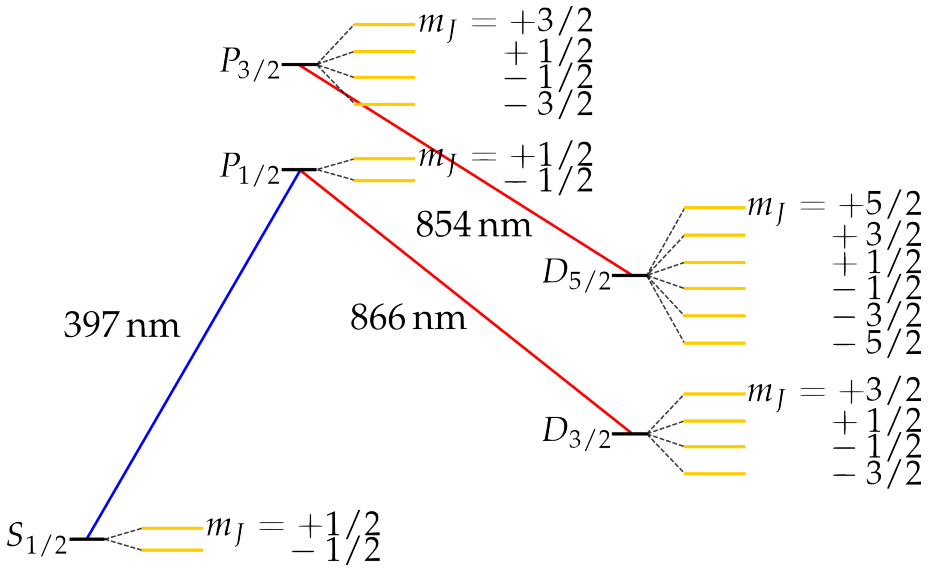

Figure 2.7: Electronic structure of $^{40}Ca^{+}$ and Zeeman splitting. The black lines are the electronic levels in the absence of magnetic field and the yellow ones are the sublevels that appear due to Zeeman splitting. The blue line indicates the transition utilized for Doppler cooling, while the red ones indicate transitions that are also needed if the cooling process is interrupted when the D states are spontaneously populated (see text). The energies are not scaled.

non-zero, resulting in a branching ratio [30]

$$\frac{P\left(P_{1/2} \to S_{1/2}\right)}{P\left(P_{1/2} \to D_{5/2}\right)} \simeq 4.2 \times 10^{-7} B^2\,\mathrm{T}^{-2}\,. \tag{2.17}$$

Under the conditions of the experiment performed by D.R. Crick *et al* [30] ($B = 1\,\mathrm{T}$), this branching ratio leads to a 70% extinction of the ion's fluorescence, because the $D_{5/2}$ state is very long-lived ($\sim 1\,\mathrm{s}$). In the present case ($B = 7\,\mathrm{T}$), the effect should be even more pronounced; thus, pumping the $D_{5/2}$ level is mandatory to perform Doppler cooling.

The magnetic field also causes energy splitting. It can be shown [31] that, for $^{40}Ca^{+}$, magnetic fields well over $\sim 10\,\mathrm{T}$ can be considered as being in the so-called *weak field regime*. In this regime, the energy correction due to Zeeman effect is given by [32]

$$\Delta E = \mu_B g_J m_J B\,, \tag{2.18}$$

where $g_J = 1 + \frac{j(j+1)-l(l+1)+s(s+1)}{2j(j+1)}$ is the Landé g-factor, μ_B is the Bohr magneton, m_J is the z component of the total angular momentum and B is the magnetic field intensity. As Eq. 2.18 is m_J-dependent, each degenerate level splits in $2j+1$ sublevels, as shown in Fig. 2.7. The light frequency required to drive a transition

$|L_1, J_1, m_{J1}\rangle \rightarrow |L_2, J_2, m_{J2}\rangle$ is

$$\nu_{12} = \frac{E_2 - E_1}{h} = \frac{\left(E_2^0 + \Delta E_2\right) - \left(E_1^0 + \Delta E_1\right)}{h} = \frac{E_2^0 - E_1^0}{h} + \frac{\Delta E_2 - \Delta E_1}{h} = \\ = \nu_0 + \frac{\mu_B B}{h}\left(g_{J2} m_{J2} - g_{J1} m_{J1}\right) = \nu_0 + K\left(g_{J2} m_{J2} - g_{J1} m_{J1}\right) , \quad (2.19)$$

where $K = 97.974\,\text{GHz}$ (for $B = 7\,\text{T}$), E_1^0 and E_2^0 are the unperturbed energies, and ν_0 is the frequency of the transition in absence of magnetic field. Eq. (2.19) will be used for the transitions' frequencies calculation, using the corresponding ν_0 obtained from the Paul trap experiment [35].

There are multiple possible choices to allow pumping all the 10 metastable $^2D_{3/2}$ and $^2D_{5/2}$ sublevels, as well as access to the cooling transition from the two $^2S_{1/2}$ sublevels. However, not all of them are experimentally feasible in the laboratory at the University of Granada, due to limitations in the number of lasers. There are enough 397 nm and 866 nm lasers in the laboratory to address each $S_{1/2}$ and $D_{3/2}$ sublevel separately, but there are only two 854 nm lasers. The frequencies for the rest of the 854 nm transitions can be obtained from sidebands using an *Electro-Optical Modulator* (EOM) [33], but they must be grouped in two triplets of equidistant frequencies. Taking this and other considerations regarding polarization and directionality (see Sec. 2.2.3) into account, the scheme shown in Fig. 2.8 is designed. Thus, the frequencies to address the cooling transition are

$$\left|^2S_{1/2}, -1/2\right\rangle \rightarrow \left|^2P_{1/2}, -1/2\right\rangle \Rightarrow \nu = \nu_B - \frac{2}{3}K = 755.157429\,\text{THz} \quad (2.20a)$$

$$\left|^2S_{1/2}, +1/2\right\rangle \rightarrow \left|^2P_{1/2}, +1/2\right\rangle \Rightarrow \nu = \nu_B + \frac{2}{3}K = 755.288061\,\text{THz} \quad (2.20b)$$

for radial access[2] and

$$\left|^2S_{1/2}, -1/2\right\rangle \rightarrow \left|^2P_{1/2}, +1/2\right\rangle \Rightarrow \nu = \nu_0 + \frac{4}{3}K = 755.353377\,\text{THz} \quad (2.21a)$$

$$\left|^2S_{1/2}, +1/2\right\rangle \rightarrow \left|^2P_{1/2}, -1/2\right\rangle \Rightarrow \nu = \nu_0 - \frac{4}{3}K = 755.092113\,\text{THz} \quad (2.21b)$$

for axial access. $\nu_0 = 755.222745\,\text{THz}$ is the frequency of the cooling transition in the absence of magnetic field.

[2]Notation: $\left|^{2S+1}L_J, m_J\right\rangle$

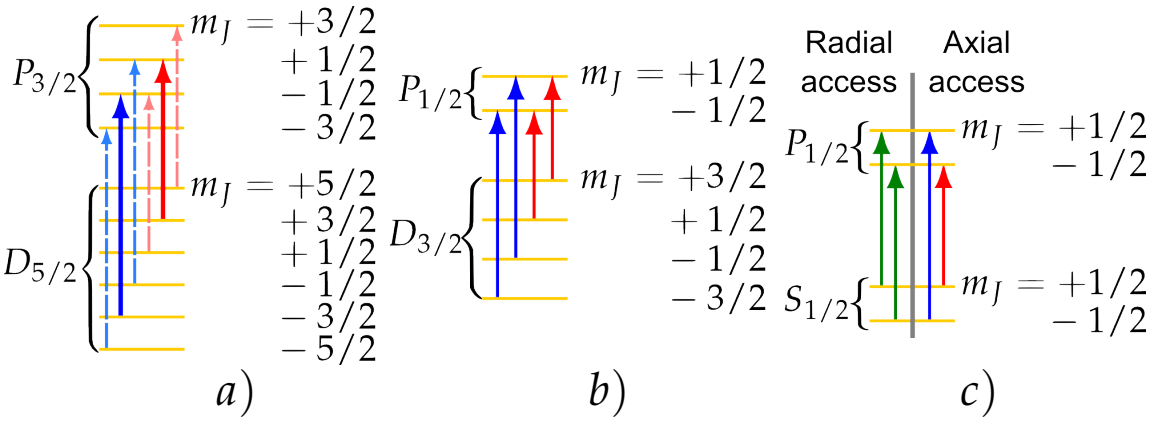

Figure 2.8: Left: transitions to pump the $^2D_{5/2}$ level. Two 854 nm lasers are set to the frequencies obtained from the energy difference between the sub-levels marked by the thick-solid arrows. The frequencies for the rest of the transitions, marked with light-dashed arrows, are the red and blue sidebands, generated after the carriers are passed through an EOM. Center: transitions to pump the $^2D_{3/2}$ level. Each frequency is generated independently by one diode laser. Right: transitions for Doppler cooling. Two schemes are shown, depending whether the laser beam is in the axial or radial direction. In all cases, red and blue arrows correspond to transitions with $\Delta m = \pm 1$ ($\sigma^{\pm}$-type transitions), respectively. The transitions where $\Delta m = 0$ (π-type transitions) are represented by green arrows.

The frequencies of the lasers to pump the $^2D_{3/2}$ sublevels are

$$\left|^2D_{3/2}, -3/2\right\rangle \rightarrow \left|^2P_{1/2}, -1/2\right\rangle \Rightarrow \nu = \nu_0 + \frac{13}{15}K = 346.085221\,\text{THz} \quad (2.22a)$$

$$\left|^2D_{3/2}, -1/2\right\rangle \rightarrow \left|^2P_{1/2}, +1/2\right\rangle \Rightarrow \nu = \nu_0 + \frac{11}{15}K = 346.072158\,\text{THz} \quad (2.22b)$$

$$\left|^2D_{3/2}, +1/2\right\rangle \rightarrow \left|^2P_{1/2}, -1/2\right\rangle \Rightarrow \nu = \nu_0 + \frac{-11}{15}K = 345.928462\,\text{THz} \quad (2.22c)$$

$$\left|^2D_{3/2}, +3/2\right\rangle \rightarrow \left|^2P_{1/2}, +1/2\right\rangle \Rightarrow \nu = \nu_0 + \frac{-13}{15}K = 345.915399\,\text{THz}\,, \quad (2.22d)$$

where $\nu_0 = 346.000310\,\text{THz}$.

Finally, the frequencies of the lasers to pump the $^2D_{5/2}$ sublevels are

$$\left|^2D_{5/2}, -5/2\right\rangle \rightarrow \left|^2P_{3/2}, -3/2\right\rangle \Rightarrow \nu = \nu_0 + K = 350.960850\,\text{THz} \quad (2.23a)$$

$$\left|^2D_{5/2}, -3/2\right\rangle \rightarrow \left|^2P_{3/2}, -1/2\right\rangle \Rightarrow \nu = \nu_0 + \frac{17}{15}K = 350.973913\,\text{THz} \quad (2.23b)$$

$$\left|^2D_{5/2}, -1/2\right\rangle \rightarrow \left|^2P_{3/2}, +1/2\right\rangle \Rightarrow \nu = \nu_0 + \frac{19}{15}K = 350.986976\,\text{THz} \quad (2.23c)$$

$$\left|^2D_{5/2}, +1/2\right\rangle \rightarrow \left|^2P_{3/2}, -1/2\right\rangle \Rightarrow \nu = \nu_0 + \frac{-19}{15}K = 350.738776\,\text{THz} \quad (2.23d)$$

$$\left|^2D_{5/2}, +3/2\right\rangle \rightarrow \left|^2P_{3/2}, +1/2\right\rangle \Rightarrow \nu = \nu_0 + \frac{-17}{15}K = 350.751839\,\text{THz} \quad (2.23e)$$

$$\left|^2D_{5/2}, +5/2\right\rangle \rightarrow \left|^2P_{3/2}, +3/2\right\rangle \Rightarrow \nu = \nu_0 - K = 350.764902\,\text{THz}\,, \quad (2.23f)$$

where $\nu_0 = 350.862876\,\text{THz}$. These can be grouped in two triplets (Eqs. 2.23a-2.23c and Eqs. 2.23d-2.23f, respectively). Thus, the laser frequencies (the center of each triplet) are given by Eqs. 2.23b and 2.23d, and the sidebands are at $\pm 13.063\,\text{GHz}$.

2.2.3 Polarization and orientation of the laser beams

Given that the magnetic field axis acts as a quantization axis, defining a privileged direction in space, it is important to know the optimal directions and polarizations to drive the desired transitions. The optimum direction and polarization to stimulate a transition is identical to the directionality and polarization of the photons emitted through spontaneous decay [31]. Thus, determinating the optimal parameters it is sufficient to characterize the spontaneous emission of the ion.

The emission patterns, i.e., intensity of light emitted at a given angle α with respect to the direction of the magnetic field $\vec{B}$, are the same as those of a classical oscillating dipole (for electric dipole transitions) [31], and are shown in Fig. 2.9a. No light is emitted with $\Delta m_J = 0$ along the magnetic field axis ($\alpha = 0\,/\,180^o$). This justifies the choice of cooling transitions for axial and radial access; in both cases, the probability to induce the transition (related to the intensity of emitted light in that direction) has been maximized.

The polarization of a photon can be entirely described with a point in the Poincaré sphere (which is similar to the Bloch sphere). The sphere is shown in Fig. 2.9b. In this parametrization, $|\phi\rangle = \cos\beta\,|\updownarrow\rangle + e^{i\gamma}\sin\beta\,|\leftrightarrow\rangle$, i.e, β gives the relative amplitude between both types of polarized light and γ the phase. The optimal polarization for a given angle α between the laser beam and the magnetic field $\vec{B}$ is given, under this parametrization, by

- π-type transitions ($\Delta m_J = 0$): $\beta = 0$ (light linearly polarized along the magnetic field axis)
- σ-type transitions ($\Delta m_J = \pm 1$): $\beta = \arctan\left(\frac{1}{|\cos\alpha|}\right)$. For σ^+ transitions, the optimal γ is $\gamma = 90^o$ if $0 < \alpha < \pi/2$, and $\gamma = 270^o$ otherwise. For σ^- transitions, the behavior is the opposite.

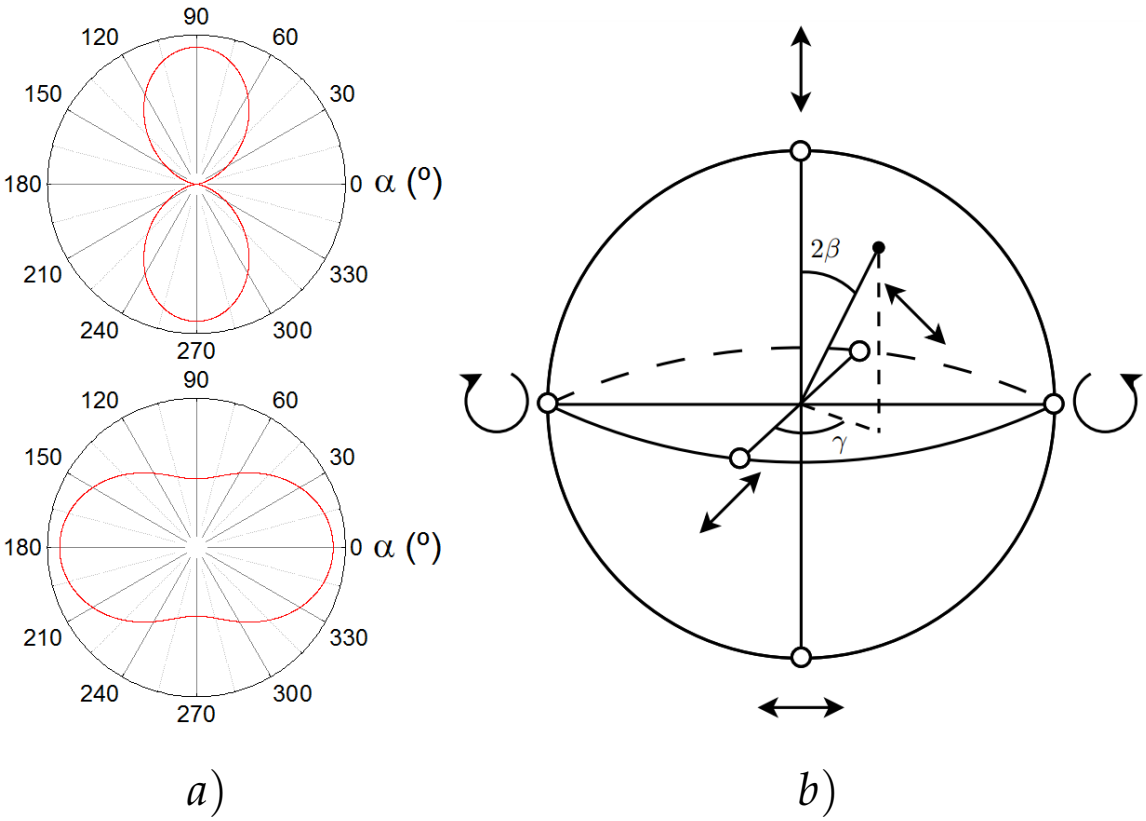

Figure 2.9: Left: radiation emission patterns for π-type ($\Delta m_J = 0$) transition (top) and $\sigma^{\pm}$-type ($\Delta m_J = \pm 1$) transition (bottom). α is the angle between the laser beam and the magnetic field. Right: Poincaré sphere (taken from [31]).

It is interesting to study the limiting cases for $\sigma^{\pm}$ transitions:

- $\alpha = 0$, 180° (axial access): $\beta = 45°$ (circularly polarized light).
- $\alpha = 90°$ (radial access): $\beta = 90°$ (linearly polarized light perpendicular to the magnetic field).

Thus, the optimal polarization for each laser is:

- For radial access: linear polarization, along the magnetic field axis for π-type transitions (cooling lasers) and perpendicular to the magnetic field for $\sigma^{\pm}$-type transitions (pumping lasers).
- For axial access: circular polarization for all laser beams. The left/right handedness depends on whether the transitions is σ^{+} or σ^{-} and α equals 0 or 180°.

Chapter 3

Experimental setup and results

This chapter is devoted to describe the experimental setup and to present the results obtained so far with a novel open-ring Penning trap. This is the first Penning trap of this kind that has been built. The setup for laser cooling in the 7 T magnetic field and the optical system to collect the fluorescence photons, implemented within this work, will be also described and characterized for the measurements. Finally, Doppler cooling of the axial motion will be addressed, using the results obtained with a radiofrequency trap. The outcomes can be projected directly to the studies with a Penning trap, since the axial motion does not depend on the magnetic field.

3.1 The Penning-traps beamline

The TRAPSENSOR facility is comprised of an open-ring Paul trap [35], which is used as test bench, a Penning-traps beamline, a laser system based on diode lasers, a Ti:Sa laser, a frequency comb and a cold-head system to cool down via helium compression to 4 K. The Penning-traps beamline, where the work presented here was carried out, is shown in Fig. 3.1. It is comprises several elements:

- A versatile laser-desorption ion source that provides the ions for the Penning-trap experiments. The ions are created when a 532-nm laser pulse hits a metallic sample. The energy of the pulses (up to 200 mJ) is focused in a small spot of the sample, originating a plasma. The singly-charged ions in the plasma are extracted using electrostatic fields.

  Although only $^{40}Ca^{+}$ ions are used in this work, samples of Re, Au, Os and other metals have also been used [21]. A sample of ^{48}Ca was recently

provided by GSI (Darmstadt, Germany) and will be used in future experiments.

- Transfer section: the ions are transported from the ion source to the Penning traps using Einzel lenses and electrostatic steerers, which are numbered correlatively starting from the ion source. The Einzel lenses are hollow cylinders with an inner diameter of 48 mm and gaps of $\sim$ 8 mm. Three Einzel lenses, with the central one at a given potential and the other two at ground, give rise to a net effect of focusing the ion beam. The steerers are made up of four independent plates; applying a negative potential to one of them results in an attractive force that steers the ion beam. A modification on the transfer section was done throughout this work (see the orange-framed inset in Fig. 3.1 and Sec. 3.1.1).

- 7 T magnet and traps: the superconducting magnet (Agilent 7T/160MM AS) houses a CF100 to CF160 vacuum tube, inside of which, the Penning traps are placed:

  - Preparation Penning Trap (PPT): this is a trap made of a stack of electrodes with cylindrical geometry (see the blue-framed inset in Fig. 3.1), which was designed and characterized with the laser desorption ion source in a previous work [21]. In the work presented here, the PPT was used to cool and purify the $^{40}Ca^{+}$ ion beam, using the buffer-cooling technique described earlier in this work (see Sec. 2.1.2). The buffer gas is helium, as its low mass enhances the energy transfer by collisions. This trap delivers the ions of interest for experiments in similar conditions as any other PPT in a radioactive beam facility.
  - Measurement Penning Trap (MPT): the second trap has a novel geometry (open-ring geometry) and will be described in detail in Sec. 3.1.2.

- TOF section: the ions extracted from the traps are transported towards a detector by means of several Einzel lenses.. The Einzel lenses are connected to a potential divider, so only one potential has to be set in this section; for all the measurements presented in this work, $V_{L\,TOF} = -20$ V.

  The detector (TOPAG MCP 25-10) is made of two micro-channel plates in chevron configuration, to which a negative potential is applied; usually, this potential is $V_{det} = -2200$ V.

The timings used to perform a TOF-ICR measurement with this setup are shown in Fig.3.2. From the laser shot, that serves as trigger, the $^{40}Ca^{+}$ ions take typically

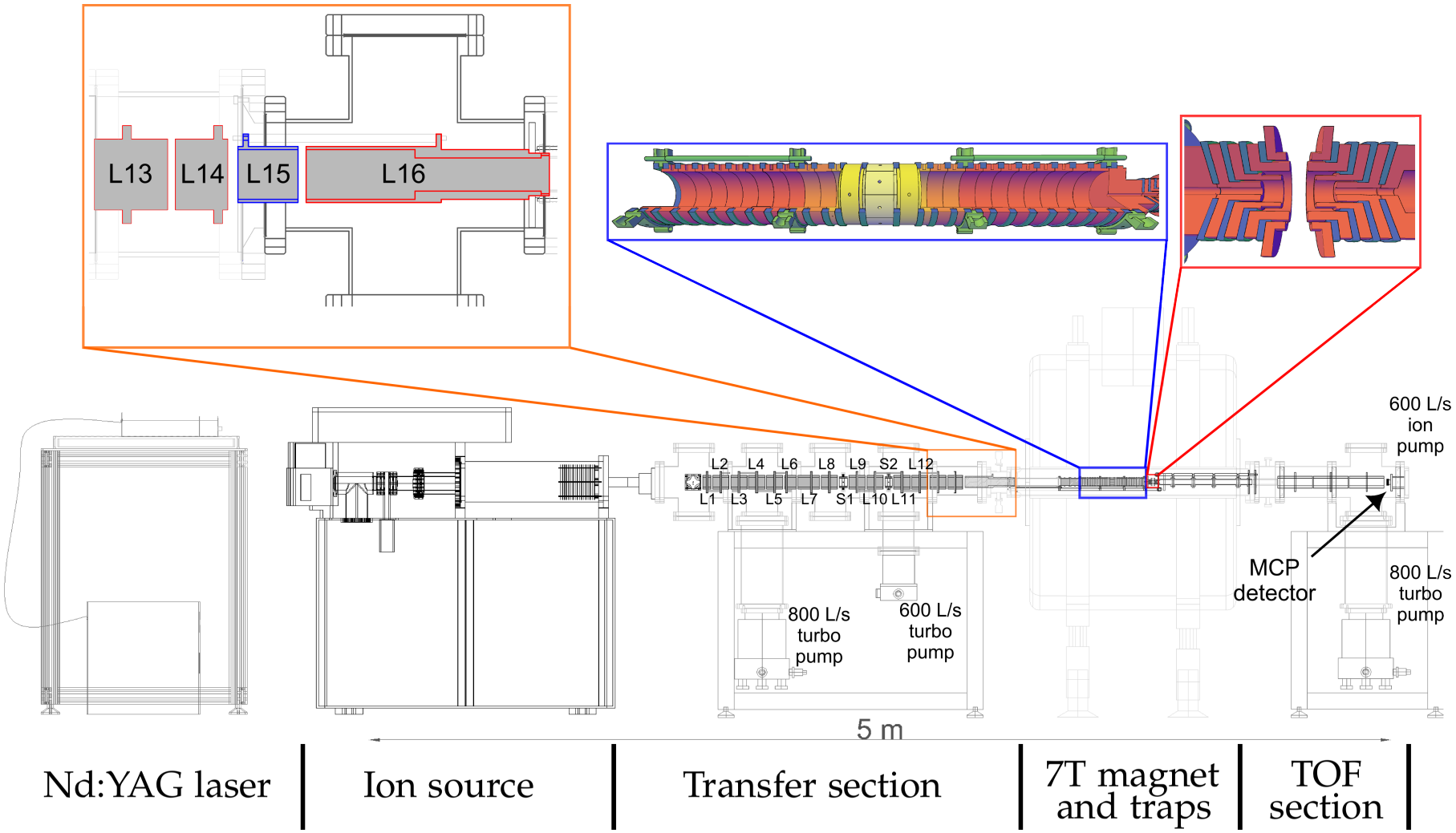

Figure 3.1: Technical drawing of the Penning-traps (PT) beamline. Left inset (orange-framed): detail of the modifications of the transfer section carried out during this work. The new CF100 vacuum cross is shown in black, and the new Einzel lens (L15) in blue. L13, L14 and L16 had to be adapted to fit within the space. Central inset (blue-framed): detail of the Preparation Penning Trap (PPT). Some electrodes have a wedge excluded for better visualization. Right inset (red-framed): detail of the Measurement Penning Trap (MPT) showing a 3D view, with a wedge excluded for better visualization.

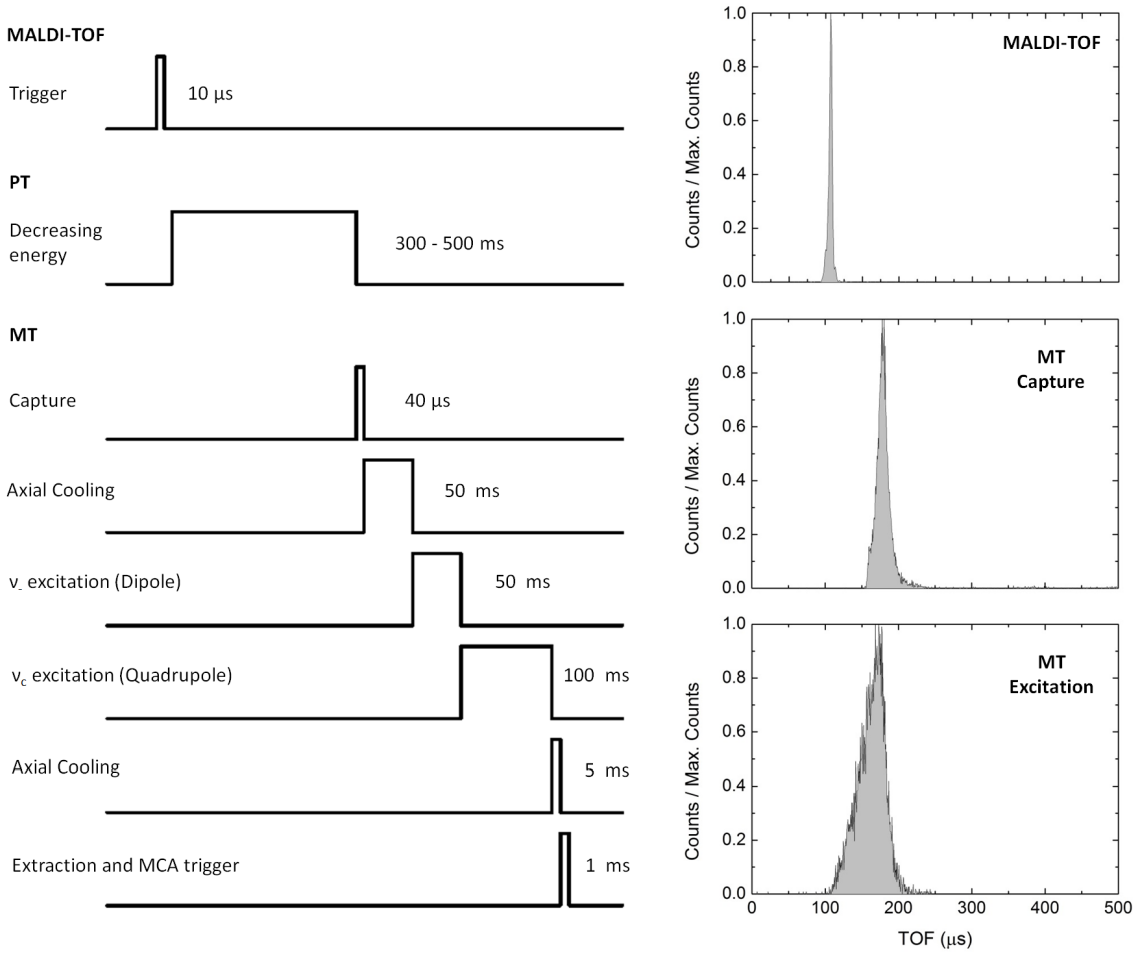

Figure 3.2: Timings used to perform a TOF-ICR measurement. The trigger of the full cycle starts when a small fraction of the laser beam is detected with a photodiode. The ions take $\sim 115\,\mu$s to reach the PPT, where a cooling resonance [21] is used to cool and filter them. They are then transferred to the MPT, with a time of flight between traps of $\sim 45\,\mu$s. The ion signals recorded with the MCP detector at the end of the beamline are shown in transmission, after the PPT and after the MPT, on the right side. From top to bottom, the acquisition is triggered with the laser pulse, the extraction from the PPT and the extraction from the MPT, respectively.

$\sim 115\,\mu$s to reach the PPT. Once they are cooled (see Ref. [21] for details), they are transfered to the MPT. The time of flight between traps for $^{40}Ca^{+}$ ions is $\sim 45\,\mu$s. Once they are trapped in the MPT, the TOF-ICR technique is applied (see Sec. 2.1.2).

3.1.1 Modifications to the setup and commissioning

Several modifications have carried out in the Penning-traps beamline and in the lasers system as previous steps towards Doppler cooling. They will be analyzed in this section.

New Einzel lenses

The first modification carried out was to replace the connection system for the PPT, to facilitate the positioning of the full traps tower inside the magnet bore. There are in total 63 connections in the magnet. The vacuum cross housing the connection plugs was replaced by a standard 6-way CF100 vacuum cross made of 316LN, that accounts for 43 of the 63 connections. This in turn forced the modification of the last Einzel lenses in the transfer section and the inclusion of a new one (see the orange-framed inset in Fig. 3.1). The new and the modified Einzel lenses were designed during this work.

An important part of this work was the alignment of the traps with respect to the magnetic field axis when the new open-ring trap was coupled. This was also followed by the optimization of the transfer section.

Magnetic field alignment

Misalignment of the magnetic field with the electrostatic potential of the traps can cause shifts in the trapped ion's observable frequencies [23] and ion losses due to collisions with the electrodes, as the ions tend to follow the magnetic field lines.

The vacuum tube that contains the traps with respect to the magnetic field, can be oriented in the magnet bore using the support structure shown in Fig. 3.3a. Turning the screws (depicted in red) moves the supports (in blue), which, in turn, move the frame (depicted in black) of the vacuum tube housing the traps. Assuming that it is possible to measure the displacement of the structure along the screws with $1.0(5)$ mm precision, the tube's position and its angle can be shifted in $0.34(17)$ mm and $0.036(18)^{o}$ steps, respectively (in both vertical and horizontal directions).

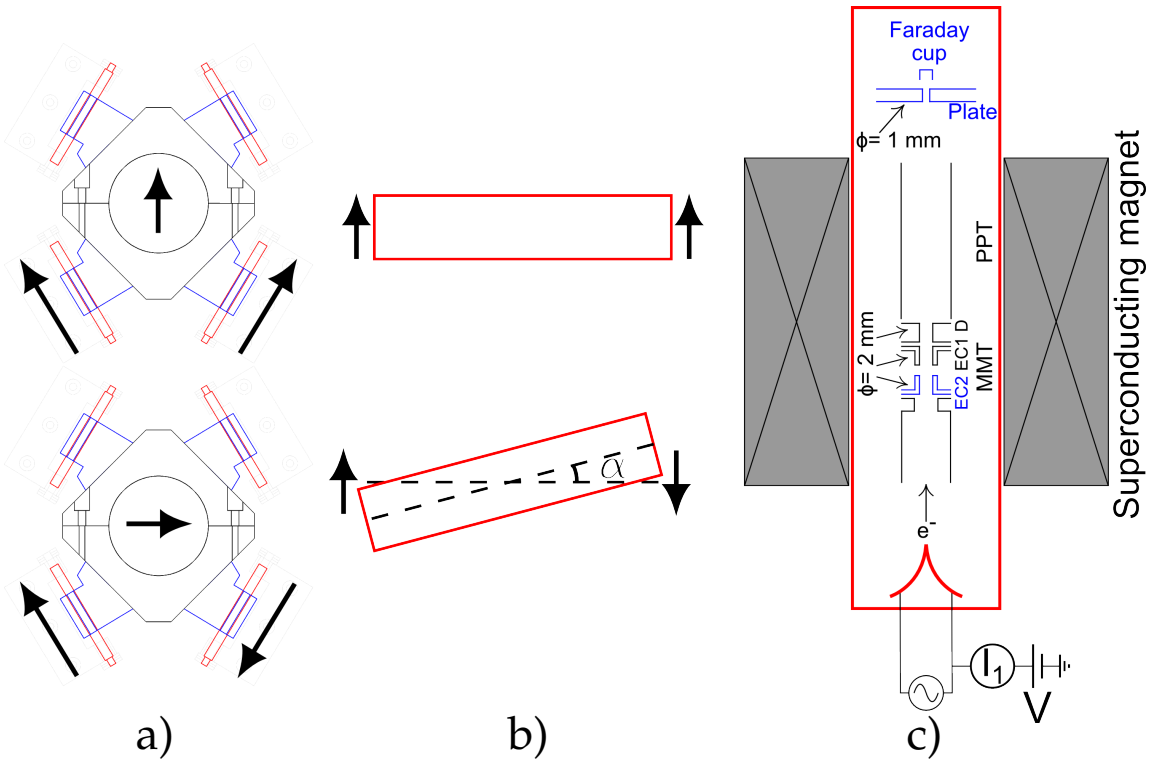

Figure 3.3: Left: technical drawing showing a front view of the system utilized to fix and align the vacuum tube housing the trap with the magnetic field. There is lateral or vertical displacement of the end of the tube depending on whether the supports move in the same or opposite directions. Center: movement of the tube as a whole. If both ends move in the same direction, a displacement is achieved; if they move in opposite directions, the angle is modified. Right: Sketch of the alignment setup using electrons emitted from a filament, depicted in red. The electron current is monitored at several locations, colored in blue.

The alignment setup is shown in Fig. 3.3c. An electron-emitting filament, shown in red, is fixed to the vacuum tube so that the emitted electrons, once collimated, are parallel to the walls. The filament is driven with an AC current, causing the electron emission, and is floated to a potential V that defines the electron's kinetic energy. The current that goes through the DC potential source (I_1 in Fig. 3.3b) is the total electron current emitted by the filament.

A plate with a 1 mm hole is placed at the other side of the magnet, and a Faraday cup is fixed behind it. These points, together with the first electrode of the MPT, called *EC2*, are used to pick up the current.

The alignment procedure consists of measuring the current at the places to pickup the current by scanning the position and angle of the tube in order to obtain the maximal current in the Faraday cup; this will indicate that the traps are optimally aligned. Two common ammeters and a picoammeter (Keithley 6285) are used for this purpose. One of the ammeters is used to continuously

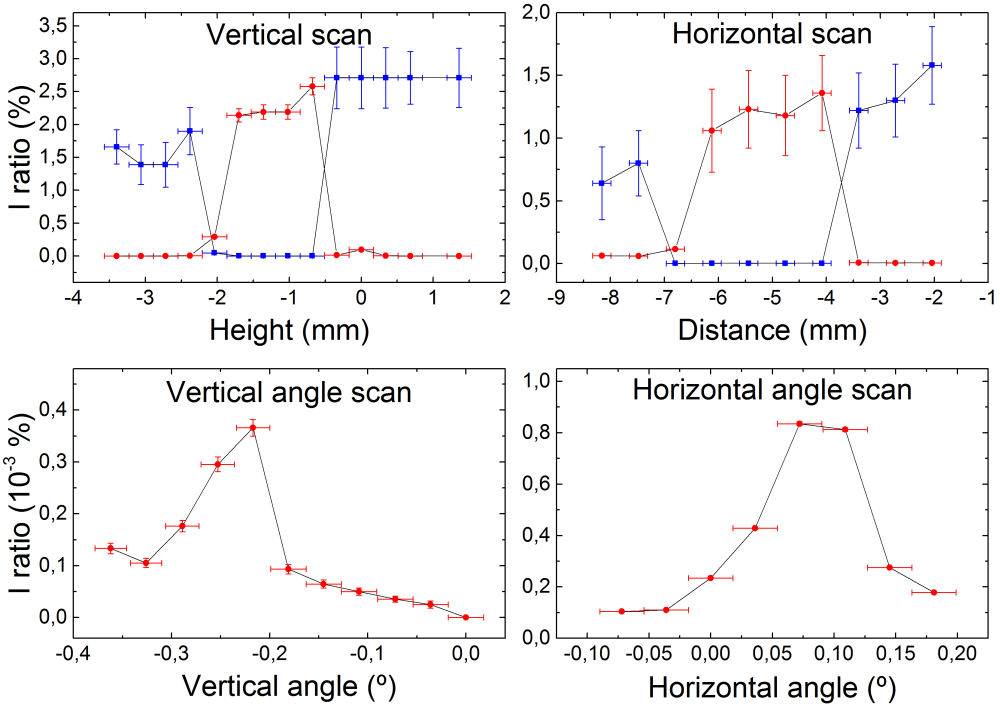

Figure 3.4: Results of the measurements carried out to align the traps with the magnetic field. Upper part: The red circles and blue squares represent the current registered in the plate and EC2, respectively. Lower part: current measured in the Faraday cup. The horizontal and vertical displacements are relative to the geometrical center of the superconducting magnet.

monitor the total emission current from the filament. The remaining ammeter and the picoammeter are used to measure the currents at the different places. The picoammeter is more sensitive, so it can measure smaller currents.

The results from the alignment are shown in Fig. 3.4. Current ratios are plotted instead of absolute currents, because all currents are normalized to the total emission current, and are thus free of fluctuations. The resulting optimal parameters are a height and lateral displacement of $-0.68(17)$ mm and $-6.12(17)$ mm, respectively, and vertical and horizontal angles of $-0.217(18)^{o}$ and $0.072(18)^{o}$, respectively.

Transfer line optimization

Once the new Einzel lenses were installed and the magnet was realigned, it was necessary to optimize the potentials in the transfer section. The number of ions detected at the end of the beamline in transmission (no trapping) is measured as a function of the potentials applied to the lenses. The potentials applied to the steerers are also optimized.

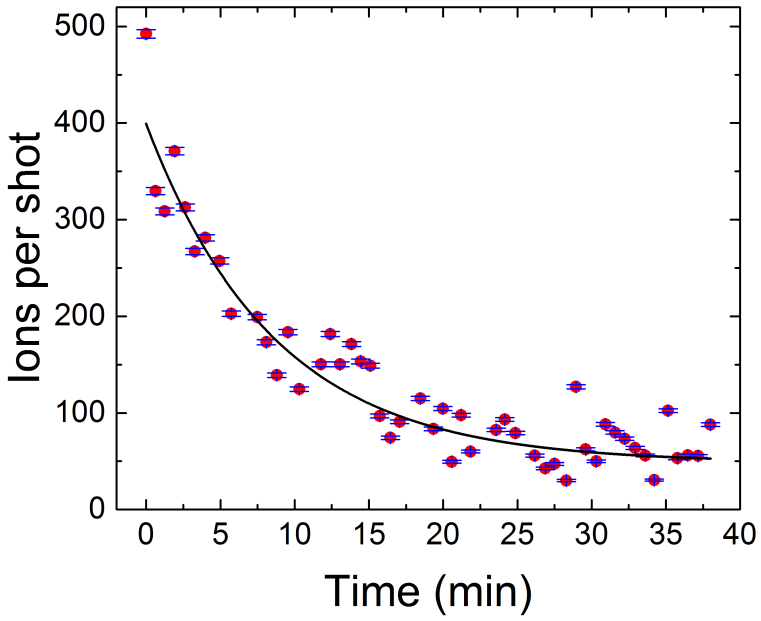

Figure 3.5: Stability of the ion source. The red circles are the average of 25 shots, and the black line is an exponential fit meant to guide the eyes.

A measurement of the number of ions vs. time is shown in Fig. 3.5. It is clear that over long periods of time the number of counts behaves like an exponential. This is presumably due to instabilities of the laser power. Each measurement averaged enough laser shots.. The results for the most significant elements are presented in Fig. 3.6.

The optimized potentials are:

$$V_{L1} = -150\,\mathrm{V} \quad V_{L3} = V_{L5} = V_{L7} = V_{L15} = 0\,\mathrm{V} \quad V_{L9} = -25\,\mathrm{V} \quad V_{L11} = -50\,\mathrm{V}$$

$$V_{L13} = -100\,\mathrm{V} \quad V_{S1H} = +2.5\,\mathrm{V} \quad V_{S1V} = -2.5\,\mathrm{V} \quad V_{S2H} = +2.5\,\mathrm{V} \quad V_{S2V} = -2.5\,\mathrm{V}$$

Vacuum system

Doppler cooling experiments need much better vacuum conditions than those of the experiments carried out previously in the PT beamline [21, 22], so further modifications had to be implemented in the beamline in order to reach lower pressures.

In addition to the two existing 800 l/s turbo-molecular pumps, another 400 l/s turbo-molecular pump was added (see Fig. 3.1) to improve the vacuum condi-

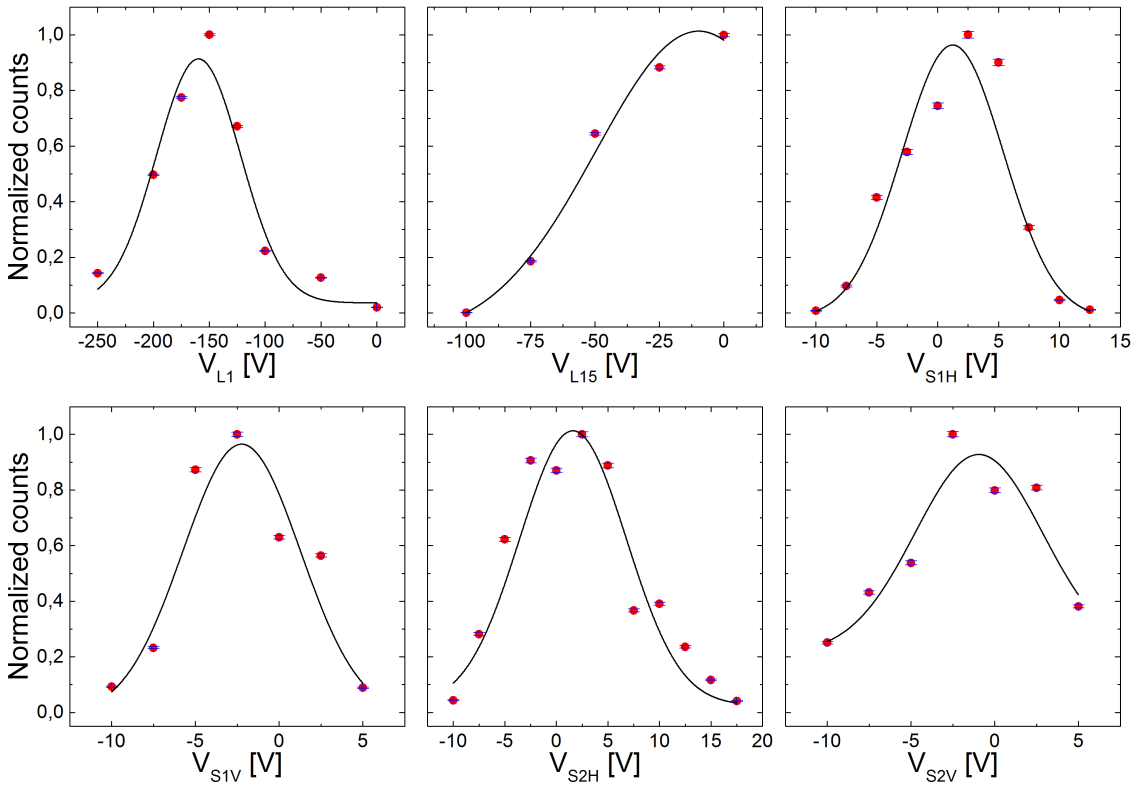

Figure 3.6: Optimization of the transfer section. The number of ion counts, represented by red-solid circles, are normalized to the maximum. Only the results from the optimization of the most significant elements of the transfer section (first and last Einzel lens and steerers) are shown. The black lines serve to guide the eyes.

tions when the PPT is operated with buffer gas. The ion pump in the TOF section, with a pumping speed of 300 l/s, was exchanged by one with 600 l/s. This pump is placed close to the MPT, where Doppler cooling will take place.

3.1.2 The open-ring Penning trap

The MPT used in this work has a novel geometry compared to any other one used before, and it was tested for the first time in Granada within this work. The trap is formed of two sets of concentric rings, centered on the beam axis (magnetic field direction). This geometry has many advantages, the main ones being:

- It is possible to trap ions created outside of the trap, as long as they are injected along the symmetry axis. This is also possible in cylindrical geometries, such as the PPT used in this work, but it is not possible in other geometries.

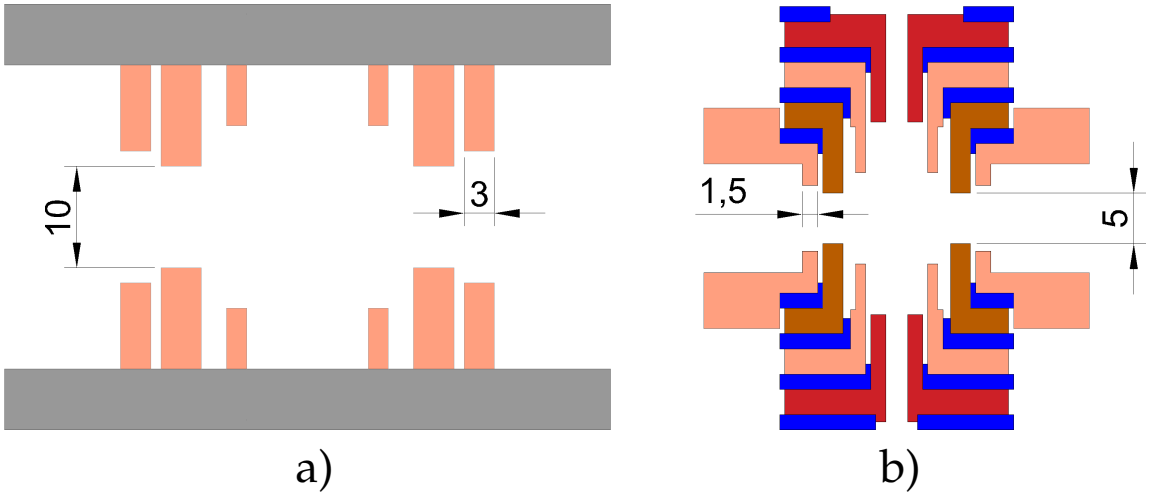

Figure 3.7: Left: Cut of the original open-ring trap [34, 35] showing the electrodes in orange and the support structure in gray. Right: Cut of the open-ring trap scaled down by a factor of 2 and with an additional electrode. The electrodes are colored in orange, brown (four-fold segmented) and red (additional one), and the isolating pieces in blue. Some distances are quoted as a reference, with dimensions in mm. The symmetry axis of the two traps is in the vertical direction.

- It offers optical access through the full radial plane. This is not possible in cylindrical traps, where holes must be made in the electrodes in order to allow radial access of lasers and fluorescence collection, resulting in electric field imperfections that have to be corrected.

The open-ring trap used in this work is a factor of two scale-down version of a previously existing one operated as a Paul trap (see Fig. 3.7a), designed originally for experiments on $\beta - \nu$ correlation [34], and where laser-cooling of a single $^{40}Ca^{+}$ ion has been demonstrated [35]. The new trap is shown in Fig. 3.7b. There is an additional electrode (depicted in red) to be used for coupling the ion to an external circuit and also to test in an intermediate step the system before the final geometry was decided [36]. In the final setup, the current induced by the trapped ion in this electrode will be used to excite a different ion confined in a twin trap that has a common electrode with the first one [18].

3.2 The laser-beams setup and the optical system

In this section, the optical setup designed and implemented in order to perform Doppler cooling in the 7 T magnetic field will be described, in particular, both the laser setup and the optical system built to collect the fluorescence photons from a laser-cooled ion.

3.2.1 Generation, stabilization and transport of the 12 laser beams

There are eight External Cavity Diode Lasers (ECDL) in Litrow configuration [37] used for Doppler cooling in the magnetic field within the TRAPSENSOR project:

- $3 \times 397\,\text{nm}$ diode lasers to drive the cooling transitions, and are usually referred to as 'blue' lasers. One of them is reserved for the Paul trap experiment.
- $4 \times 866\,\text{nm}$ diode lasers to drive the $^2D_{3/2}$ pumping transition, one for each sublevel, and are usually referred to as 'red' lasers.
- $2 \times 854\,\text{nm}$ diode lasers to drive the $^2D_{5/2}$ pumping transition. Since one needs six for the $^2D_{5/2}$ sublevels, an EOM is used to generate sidebands (see Sec. 2.2.2). These are also referred to as 'red' lasers.
- A He-Ne laser used for wavelength calibration.

The relevant elements comprising the laser setup for cooling are shown in Fig. 3.8. All the diode lasers emit linearly polarized radiation in a given direction. A beamsplitter behind the laser head reflects only 10% of the laser power (90/10 BS), which is introduced into an optical fiber that transports the laser light to a wavelength meter using a mechanical switch. The wavemeter is calibrated with the 632-nm transition from a HeNe laser. The measurements of the wavelengths are compared sequentially with a given value, and the deviations are corrected sending an electronic signal to a piezo which acts on the grating of each laser cavity, thus modifying the frequencies accordingly. The control is a closed-loop PID regulation system and the software was developed as part of a different Master Thesis, where it is described in detail [38].

The largest fraction of the laser power (90%) is used for the experiment. The orientation of the polarization of the laser beams is tuned with a half-wave plate. One blue laser is polarized horizontally and the other vertically before they are coupled into polarization maintaining optical fibers. Both are combined in a Polarizing Beam Splitter (PBS) built in in cube with three fiber couplers (2 IN and 1 OUT).

In the red lasers' case, a $\lambda/2$ plate is also placed behind the 90/10 BS. The 866 nm lasers are combined in pairs of the same polarization using a 50/50 BS and then introduced into optical fiber. Both beams can then be combined in a fiber PBS.

The 854 nm lasers, on the other hand, are combined in a PBS after the $\lambda/2$ plates and feed an Electro Optical Modulator (EOM) via an optical fiber. This device has been studied and characterized for a driving field of 40 GHz in a previous

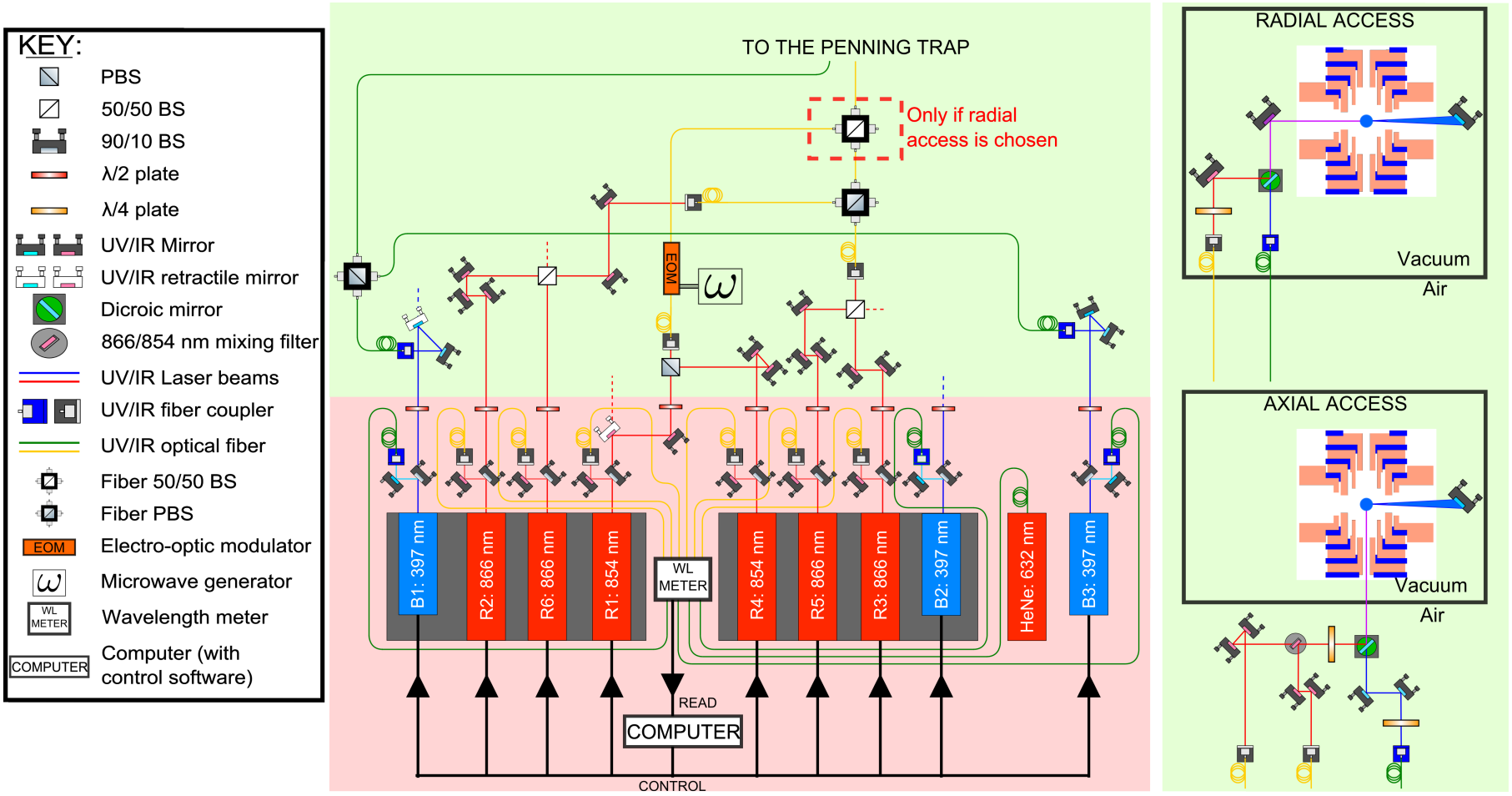

Figure 3.8: Laser setup. The previously existing part is shaded in red, and the new developments, devoted to perform Doppler cooling in the Penning trap, are shaded in green. The laser beams are combined as shown in the figure (see text for details) and then transported to the MPT via optical fibers. The right side of the figure shows two possibilities to access the ions with the laser beams: radially (top) and axially (bottom). The fluorescence is always collected radially.

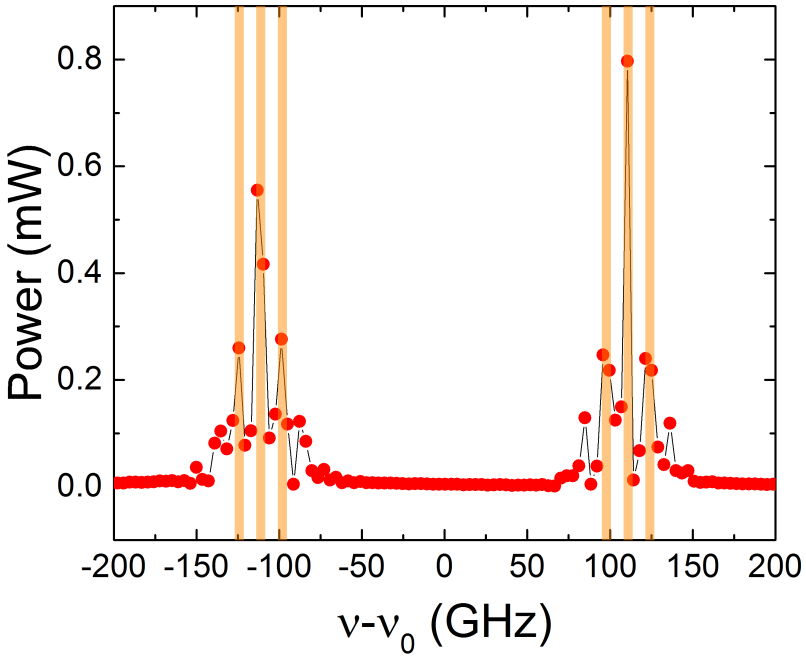

Figure 3.9: Generation of the sidebands from two carrier frequencies around 854 nm laser light, using an EOM. The orange lines mark the laser frequencies required to pump the 6 metastable $^2D_{5/2}$ sublevels as shown in Sec. 2.2.2. The frequencies are given with respect to the transition frequency in absence of magnetic field (ν_0).

Master Thesis [33]. In the EOM, when laser radiation at a given frequency ν is introduced and radio-frequency field at ν_{RF} is applied, sidebands at $\nu \pm n\nu_{RF}$ appear. The power of the radiation at the input frequency (*carrier*) and at the sidebands depends on the radio-frequency's amplitude according to the Bessel functions. An example is shown in Fig. 3.9; radiation of two different wavelengths is introduced in the EOM, and sidebands are generated. Choosing adequately the lasers' frequency and with suitable radiofrequency (see Sec. 2.2.2), the carriers and first sidebands have enough power to drive the six pumping transitions for the $^2D_{5/2}$ level.

The 866 nm and 854 nm beams are combined into an optical fiber BS if the radial access scheme is used (see Fig. 3.8) and introduced in vacuum. Two fiber couplers with specific lenses, one for each fiber, allow the transition from in-fiber propagation to free propagation and the focussing with the desired spot size in the center of the trap. The two beams are then combined using a dichroic mirror, and directed towards the trap's center. Figure 3.10 shows the in-vacuum laser system for radial access.

If axial access is needed, the 866 nm and 854 nm beams are transported in separated optical fibers. Three fiber couplers are used to extract the laser radiation

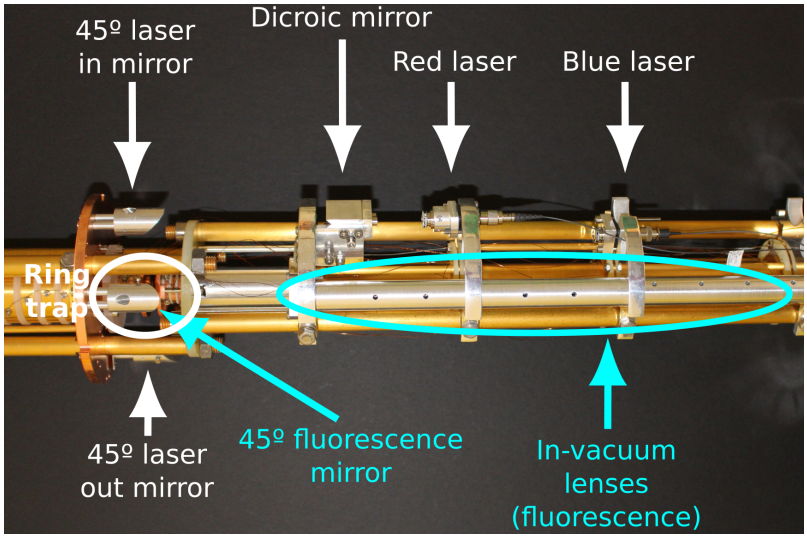

Figure 3.10: Picture of the open-ring Penning trap with details for laser access and fluorescence detection. The laser access and optical systems have been built within this Thesis. The laser beams are coupled through CF16 vacuum feedthroughs to special optical fibers designed to operate under ultra-high vacuum conditions and in high magnetic fields. The red and blue laser beams are combined in a dichroic mirror, they are reflected once to pass the trap through the center and again in another mirror to direct the beam the outside. The fluorescence emitted within a certain solid angle is diverted 90 degrees into the optical system and collimated to the EMCCD camera.

from the blue and red fibers outside the vacuum. The 866 nm and 854 nm beams are combined using a special filter that results in much less power loss than a regular BS. They are then combined with the blue beam using a dichroic mirror and introduced in the axial direction directly through a viewport, without using any optical fiber (see Fig. 3.8).

The axial access scheme is problematic, because the MCP detector interrupts the laser path. There are two possible solutions: a suitable electrostatic field can bend the ion's trajectory after they are extracted from the traps, so they no longer follow the laser's path. Other solution is to place the detector in a mobile frame. The second approach is much simpler and has been chosen for simplicity. The modifications are under way.

3.2.2 The image collection system

The ion's fluorescence is extracted radially, as shown in Fig. 3.8, independently of the laser setup chosen. A mirror is placed at 45º with respect to the axial axis to direct the fluorescence along the axial direction in parallel with the magnetic field, and then a set of lenses are placed to minimize losses; they are shown in

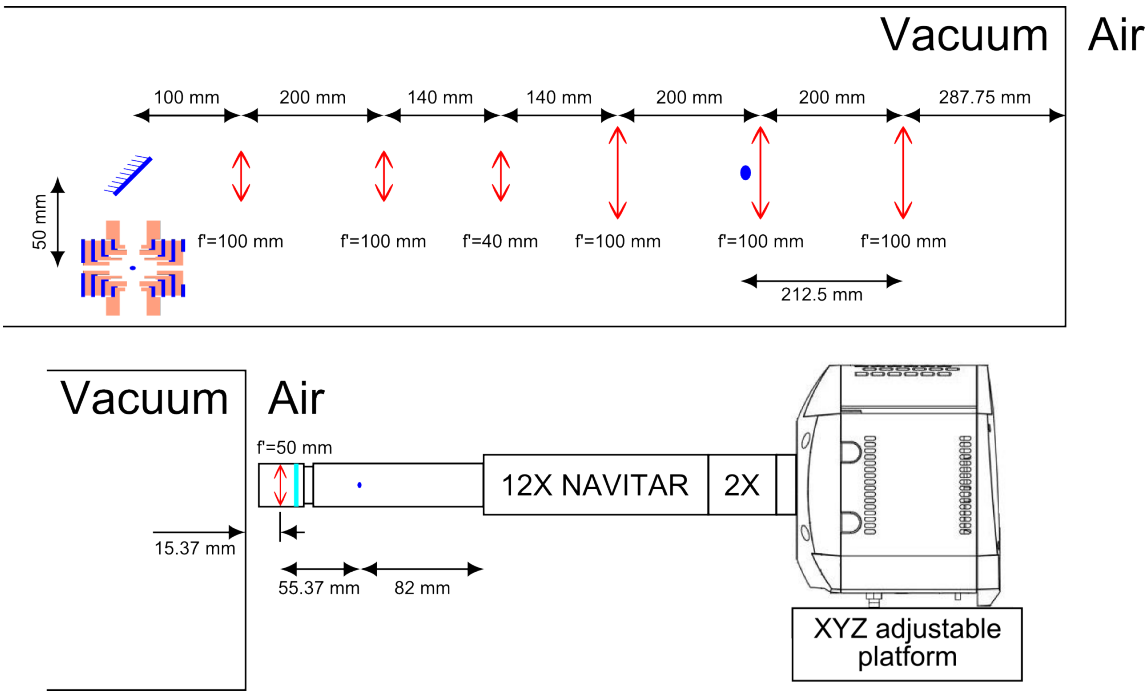

Figure 3.11: Sketch of the optical system to collimate the fluorescence photons from the laser-cooled ions.Top: Part of the system inside vacuum, which is comprised of 6 lenses, 3 of 1/2" diameter and 3 of 1" shown in red, and a mirror, shown in blue. The blue circles are the ion cloud and its image through the 6 lenses. Bottom: Part of the system outside vacuum, comprised of one lens (50 mm focal distance), an interference filter, and adjustable zoom lens $1-14$X (MVL12X12Z from Thorlabs, with the accessories MVL20A and MVLCMC) and and EMCCD camera (ANDOR iXon Ultra 888). The blue dot is the ion cloud image through the vacuum and the $f' = 50\,\text{mm}$ lenses.

Fig. 3.11 (a part of the system is also shown in Fig. 3.10).

The aerial part of the optical system was designed during this work. First, the position of an object placed in the trap's center is calculated using the thin-lens approximation,

$$\frac{-1}{s} + \frac{1}{s'} = \frac{1}{f'} \qquad \beta' = \frac{y'}{y} = \frac{s'}{s}\,, \tag{3.1}$$

where s is the distance from the object to the lens, s' is the distance from the image to the lens, y the object size, y' the image size, f' the focal distance of the lens and β' the so-called 'lateral magnification'. The sign convention given in Ref. [39] is used. This results in an image 212.5 mm left of the last in-vacuum lens, with a magnification $\beta' = -2.5$.

The commercial optical system that is attached to the camera has a working distance of 82 mm, but the minimum possible distance from the image to the

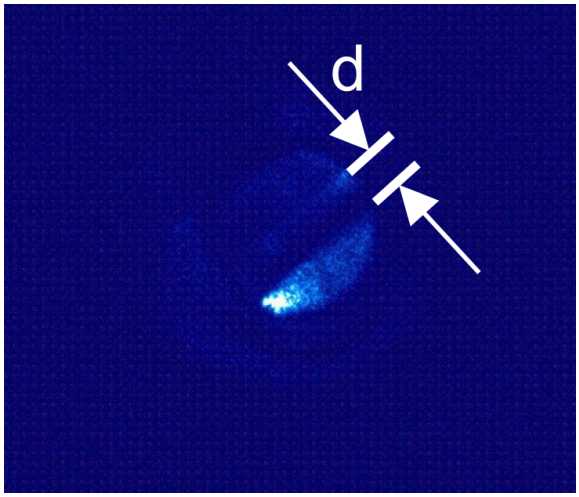

Figure 3.12: Picture of the open-ring trap obtained with the optical system designed in this work. The electrodes are illuminated by the laser light reflected in one of the mirrors surrounding the trap. The distance d marked in the picture is the distance between the electrodes.

optical system is $212.5 + 287.75 \simeq 500\,\text{mm}$; thus, additional elements must be used in order to obtain an image. The experimental approach is to place a lens with $f' = 50\,\text{mm}$ at 303 mm from the vacuum lenses' image, that is, at 15.37 mm from the viewport at the end of the vacuum chamber. This results in an image 55.37 mm to the right of that lens, with a global magnification $\beta' = 0.2685$. Attaching the lens to the camera and its optical system with a tube with variable length allows correcting the lens' position, and in this way the possible deviations from the calculations.

Using this system with the minimum magnification allowed by the commercial optical system (0.58x) and introducing the red laser beams, the image shown in Fig. 3.12 is obtained. Measuring the distance of the gap observed, one obtains $d = 50(12)\,\text{px} = 0.67(17)\,\text{mm}$ ($13\,\mu$m pixel size). Taking into account the global magnification ($\beta'_t = 0.2685 \cdot 0.58 \simeq 0.1557$), results in a gap $d' = 4.2(1.0)\,\text{mm}$, consistent with the distance between electrodes shown in Fig. 3.7b. Thus, one can conclude that the optical system meets the requirements to detect the fluorescence from ion clouds in the center of the trap. Since the system can provide a magnification of 12x (a $\sim$ 24 fold gain), it should be possible to observe the fluorescence from a single laser-cooled ion.

In the configuration adopted for the detection of the fluorescence photons from a $^{40}Ca^{+}$ ion, an interference filter is placed to get only the 397 nm photons from the cooled ion.

3.3 Experimental results

3.3.1 Characterization of the open-ring trap

The open-ring Penning trap has been used for the first time during this work, so it had to be commissioned and characterized. The potentials applied to the rings have to be determined. In principle, a pontential is applied only to two rings (four, taking into account the symmetry of the trap along the radial plane). The other two (four), innermost and outermost rings, remain grounded during the potential's calculation. These potentials are crucial to fix the axial frequency $\nu_z = \omega_z/2\pi = 100\,\text{kHz}$ while reducing the anharmonicities to the lowest possible level. This method was described in a PhD thesis [21]. After the potential in the axial direction is close to harmonic, an offset is added to all the electrodes in order to optimize the ion transport between the PPT and the MPT; this does not distort the potential shape.

Together with the DC potential, the segmented electrodes are used to apply a dipolar field at the magnetron frequency. A dipolar field is also applied between opposite electrodes in the axial direction at ν_z. The number of detected ions versus the excitation's frequency is studied. If the frequency is close to the ion's eigenfrequency, the associated ion's amplitude increases. If the strength and duration of the amplitude of the field are adequate, the ions are lost from the trap.

The results from the application of dipolar fields at ν_z and ν_- are shown in Fig. 3.13. In the magnetron case, a reduction of the time-of-flight of the ion due to the force appearing when the ions leave the magnetic field (see Sec. 2.1.2) is also observed, as predicted from theory. This allows for a more precise determination of the magnetron frequency. The Gaussian fits shown in Fig. 3.13 result in $\nu_z = 102.42(15)\,\text{kHz}$ with $\sigma_z = 3.2\,\text{kHz}$ and $\nu_- = 3000(20)\,\text{Hz}$ with $\sigma_- = 208\,\text{Hz}$.

3.3.2 Time-of-flight resonances

The most important measurement carried out in the Penning trap is the time-of-flight resonance. As explained in the previous chapter, the magnetron motion is converted to reduced-cyclotron. In order to achieve full conversion from one to the other, the amplitude and duration of the quadrupole excitation have to be fixed properly, but these cannot be found until the cyclotron frequency is known.

In order to find the cyclotron frequency, the time-of-flight resonances were obtained as described in Fig. 3.2; the results are shown in Fig. 3.14. When the

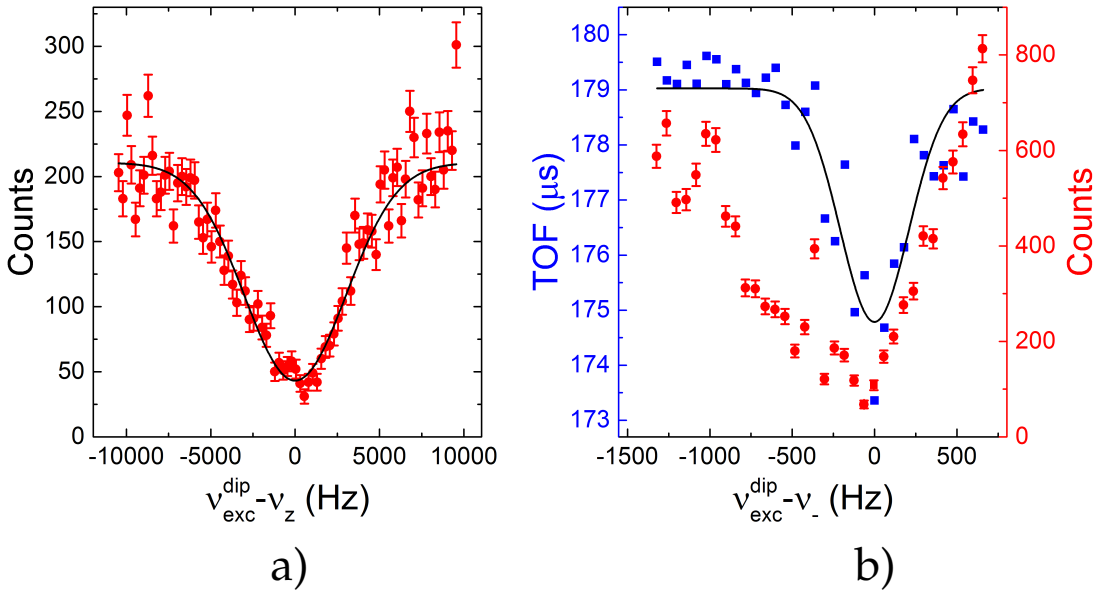

Figure 3.13: Left: determination of the axial frequency of $^{40}Ca^{+}$ in the new trap. The red circles are ion counts and the black line is a gaussian fit. Right: determination of the magnetron frequency. The red circles are ion counts, and the blue squares are the average time of flight. The black line is a gaussian fit to the TOF data points.

amplitude and duration of the excitation are not properly set the conversion is not complete, yielding deviations from the expected time-of-flight spectrum [13], although the spectrum's envelope must remain centered at ν_c. One can obtain the central frequency by fitting the envelope (a Lorentzian function provides a better result compared to a Gaussian). Calculating the weighted average of the central frequencies resulting from each of the fits:

$$\begin{cases} \nu_{50mV_{pp}} = 2.68938994(47)\,\text{MHz} & \nu_{100mV_{pp}} = 2.6893947(11)\,\text{MHz} \\ \nu_{105mV_{pp}} = 2.68938361(78)\,\text{MHz} & \nu_{300mV_{pp}} = 2.6893966(18)\,\text{MHz} \\ \nu_{400mV_{pp}} = 2.6893916(31)\,\text{MHz} & \nu_{500mV_{pp}} = 2.6893933(17)\,\text{MHz} \end{cases} \Rightarrow$$

$$\Rightarrow \begin{cases} \nu_c = \dfrac{\sum_i \left[\nu_i/(\Delta\nu_i)^2\right]}{\sum_i \left[1/(\Delta\nu_i)^2\right]} = 2.68939166\,\text{MHz} \\ \Delta\nu_c = 1/\sqrt{\sum_i \left[1/(\Delta\nu_i)^2\right]} = 0.36\,\text{Hz} \end{cases} . \quad (3.2)$$

one obtains $\nu_c = 2.68939166(36)$ MHz.

The cyclotron frequency obtained at this stage can be used to calibrate the magnetic field. Using the last available data for physical constants [40] and atomic masses [41],

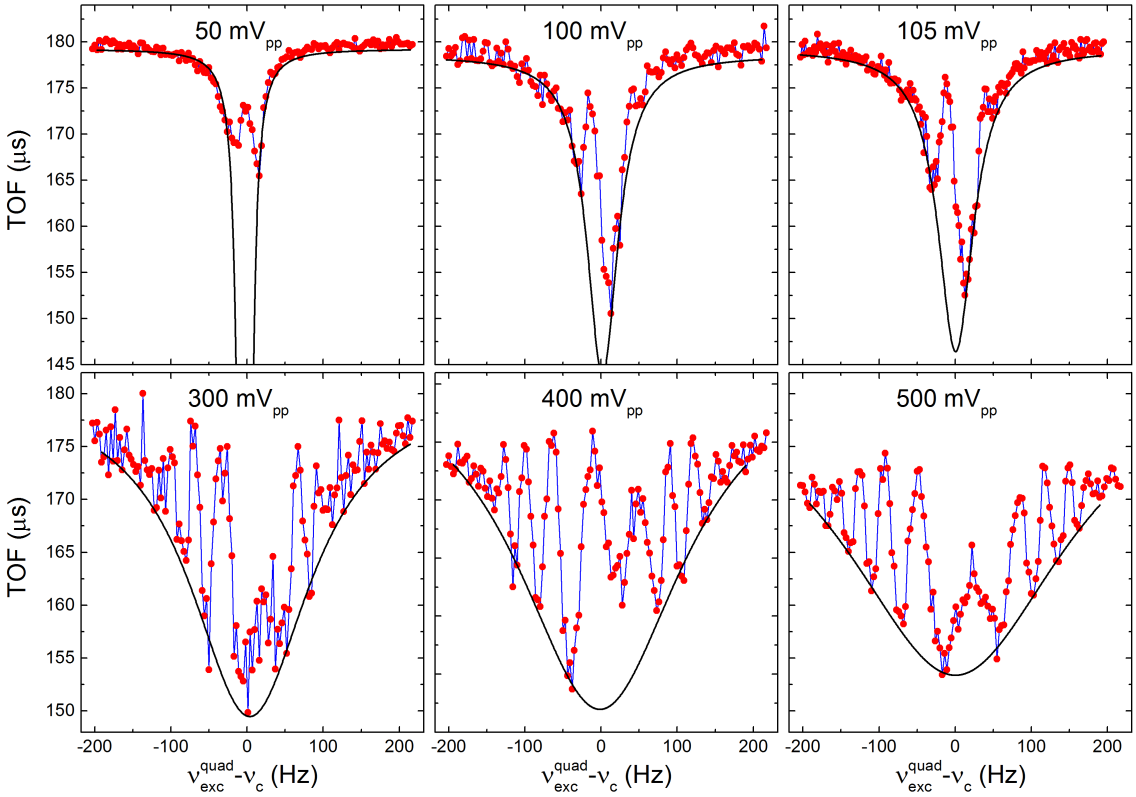

Figure 3.14: Time-of-flight spectra spectra for different amplitudes and Lorentzian fit to the envelopes. The width of the envelope increases with the amplitude making the sidebands more visible.

$$B = \frac{m_{^{40}\mathrm{Ca}^+}}{q}\omega_c = \frac{m_{^{40}\mathrm{Ca}^+}}{q}2\pi\nu_c \simeq \frac{m_{^{40}\mathrm{Ca}} - m_{e^-}}{q}2\pi\nu_c = 6.99874706(94)\,\mathrm{T}\,, \qquad (3.3)$$

where the binding energy of the last electron of the ^{40}Ca atom was not taken into account because the correction it introduces, $\delta B = 1.15\,\mathrm{nT}$, is below the uncertainty. This magnetic field value can be used to measure masses of other ion species.

Fixing ν_c, an amplitude scan with a pulse duration of 25 ms is performed. The result is shown in Fig. 3.15a. Maxima and minima in the time-of-flight appear, which correspond an ion with full magnetron and full reduced-cyclotron motion, respectively. Choosing the minimum with more data points around, the spectrum shown in red in Fig. 3.15b is obtained. The result is only symmetric for this small duration of the excitation pulse. Furthermore, in the present stage of performance, the difference between maxima and minima in the time-of-flight signal, decreases for longer excitation times. We attribute this to the background pressure, which has not yet reach an optimal value. This pressure regime does

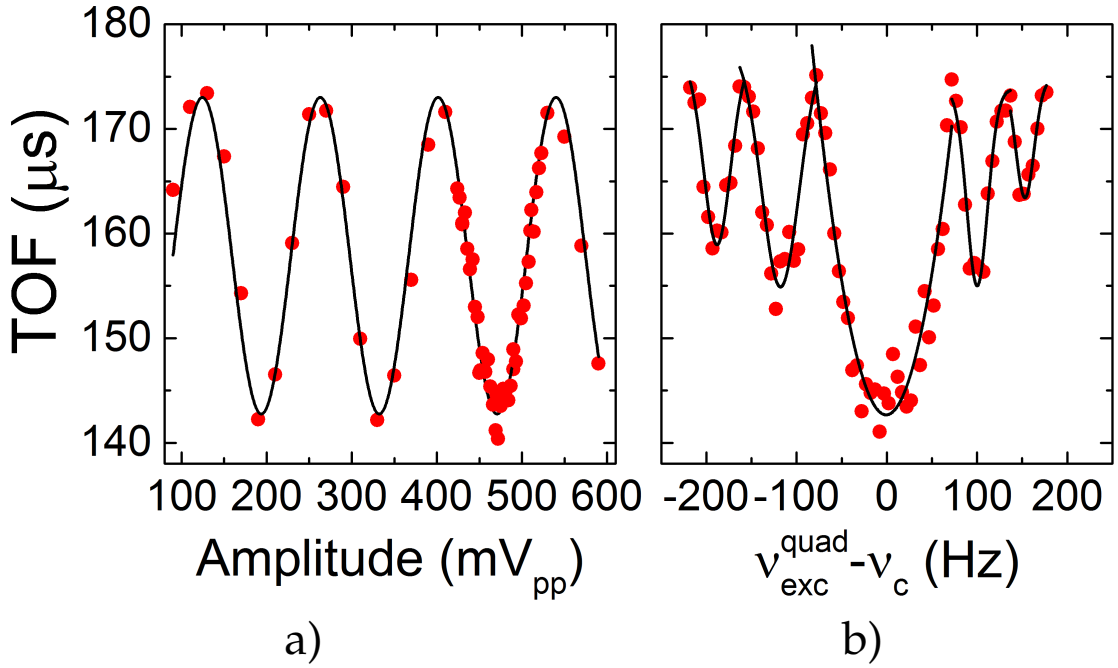

Figure 3.15: Left: amplitude scan with a pulse duration of 25 ms. The oscillation in the time-of-flight (red circles) is due to the periodic conversion from magnetron (maxima) to reduced-cyclotron motion (minima) when a quadrupole field at ν_c is applied. The black-solid line serves to guide the eyes. Right: TOF resonance for a quadrupolar excitation of 472 mV$_{pp}$ amplitude and 25 ms duration. One can see clearly the side bands. The line serves again to guide the eye.

not allow to perform laser cooling in the open-ring Penning trap at present. Work is currently on-going to overcome this.

3.3.3 The Quantum Sensor approach

With the TOF-ICR technique, it is possible to measure the mass from the determination of ν_c with a precision of 10^{-7}-10^{-8}. Using the Quantum Sensor approach, one would measure each of the motional frequencies, ν_+, ν_- and ν_z, separately. Once they are determined, the cyclotron frequency, and thus the ion's mass, can be obtained using the invariance theorem (Eq. 2.10).

In the Quantum Sensor approach one uses the laser-cooled ion as detector, although many of the steps in the measurement procedure are like those described previously. However, in this approach, all of the motions are monitored non-destructively through the axial motion of the $^{40}Ca^+$ ion. The steps for a measurement are:

1. Cool the $^{40}Ca^+$ sensor ion to the Doppler limit. The ion of interest is cooled sympathetically by coupling it to the laser-cooled ion.

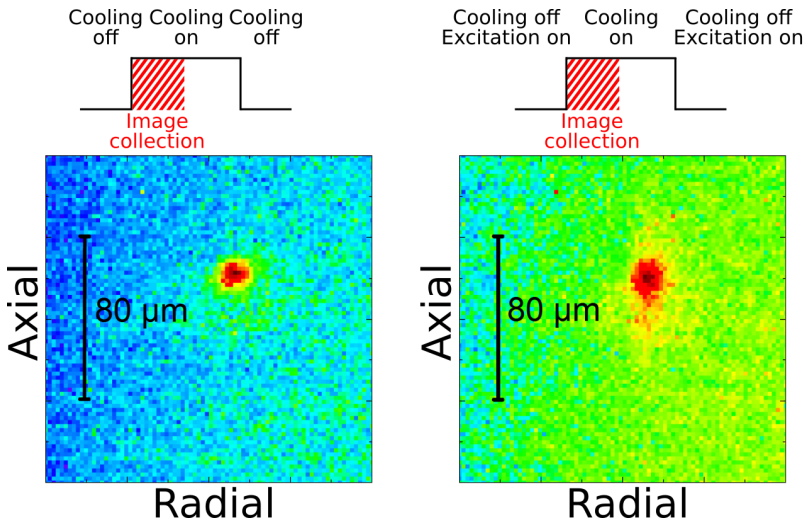

Figure 3.16: Left: fluorescence photons emitted by an ion and collected with the optical system during 75 ms. The lasers are switched off to stop the cooling, and the EMCCD camera is triggered when the cooling is resumed. Right: same procedure but applying an axial dipole oscillating field during the time the cooling is stopped.

2. Apply a dipole oscillating field, with a fixed amplitude and duration, to the ion of interest, in order to excite the desired motional frequency (ν_+, ν_z or ν_-) .

3. If the excitation is performed on the magnetron or reduced-cyclotron motion, apply a π-pulse in order to convert it to the axial motion.

4. Enable the communication between the ions by making equal their axial oscillation frequencies. The axial energy will be transferred from the ion of interest to the sensor ion.

5. Stop the energy transfer and resume the cooling, observing the energy gained by the sensor ion through the fluorescence photons.

The method is similar to the so-called "Doppler recooling" technique, which is used to determinate the heating rate of a trapped ion by measuring the energy it gains during a given time without cooling [42].

The sensitivity of a laser-cooled ion as a sensor in the TRAPSENSOR project is currently under study (see e.g. Ref. [43]). Studying the fluorescence's distribution of a single ion when a dipole oscillating field is applied, in particular, the standard deviation of the fluorescence in the axial direction, σ_z, can be used to determine the axial frequency. σ_z is related to the kinetic energy of the particle.

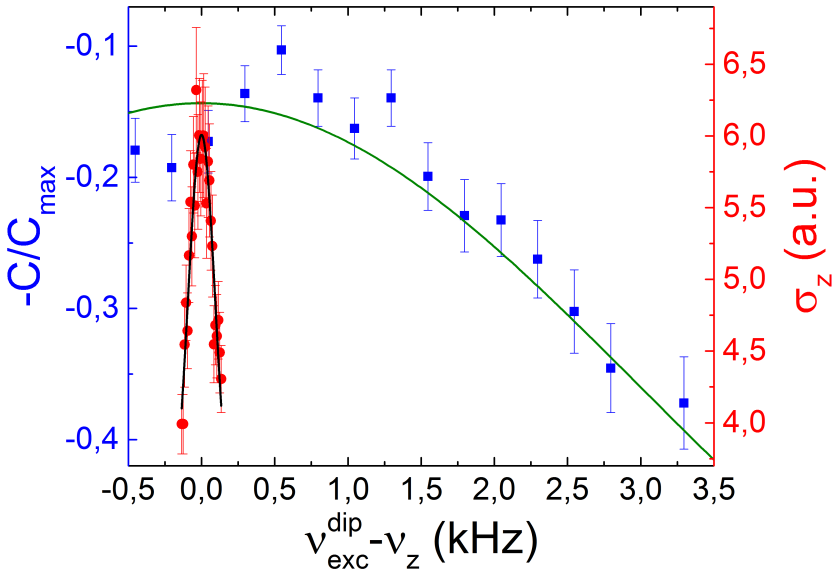

Figure 3.17: Comparison of the axial frequency determination using the micro-channel plate detector at the end of the beamline (data points in blue) and the fluorescence photons (data points in red). The fluorescence method results in $\sigma = 92\,\text{Hz}$, while the results from the previous section yield $\sigma = 3.2\,\text{kHz}$

Using the virial theorem for a quantum harmonic oscillator[1],

$$\langle K \rangle = \langle V \rangle = \frac{1}{2} m\omega^2 \left\langle z^2 \right\rangle = \frac{1}{2} m\omega^2 \sigma_z^2 \Rightarrow \langle K \rangle \propto \sigma_z^2 \ , \tag{3.4}$$

where K is the kinetic energy and V the potential energy. Thus, studying σ_z as a function of the dipole field's oscillation frequency, one can study the energy gained, which will be maximal when it matches the ion's axial frequency. Fig. 3.16a and b show the ion's image without and with dipole excitation, respectively. The fluorescence distribution in z (vertical direction) spreads when the excitation is applied.

Since the axial motion does not depend on the magnetic field, the situation is comparable to an RF trap. Comparing the determination of the axial frequency shown in the previous section, with the latest results obtained with the fluorescence method (see Fig. 3.17) in the Paul trap, it is immediately understood why the Quantum Sensor approach is so promising. There is an enormous improvement in sensitivity: while a dipolar field with $600\,\text{mV}_{\text{pp}}$ amplitude was used in the micro-channel plate approach, only $1\,\text{mV}_{\text{pp}}$ is needed to obtain the results shown in Fig. 3.17. The difference is more pronounced when taking into account that the RF trap's size doubles that of the Penning trap. The sensitivity

[1] A more rigorous proof can be given considering thermal states, but this is considered outside the present Thesis' scope.

improvement is accompanied by a much better linewith, better resolving power and better accuracy.

Chapter 4

Conclusions and outlook

In this work, the most recent developments towards Doppler cooling in a 7 T magnetic field have been presented. An open-ring Penning trap has been integrated into the Penning-traps beamline and has been tested for the first time achieving a time-of-flight resonance, which is a first step towards high-precision mass measurements. Prior to these measurements, it was necessary to study the way laser-cooling can be practicable in the 7 T field, since this is the first time in the world laser cooling will be carried out in such a high magnetic field. After deciding the electronic transitions to be used, and thus designing the laser system, the optical access for the lasers has been implemented using ultra-high vacuum optical fibers. Note that the pressure regime to accomplish laser cooling must be below 10^{-9} mbar. The open-ring trap, coupled to a laser-desorption ion source, a transfer section and a preparation Penning trap [21] located upstream, and a time-of-flight section located downstream, in front of the micro-channel plate detector, has been aligned with the magnetic field with unprecedented accuracy. The characteristic frequencies of the $^{40}Ca^{+}$ ion in the 7 T Penning trap have been determined as well as the cyclotron frequency, using the TOF-ICR technique. To get all these measurements done, it is necessary to apply all the manipulation techniques described in this work. At present, the time-of-flight measurement is limited to very short excitation times due to the vacuum conditions. This limits the accuracy that can be reached, so in this work the ν_c measurement has been used to determine the magnetic field using a more precise mass value for the $^{40}Ca^{+}$. By measuring ν_c for a few hours, the uncertainty due to magnetic field fluctuations can be studied. With respect to the vacuum improvements, it is crucial to reduce the gas flow from the preparation trap to the measurement trap. This implies the use of other cooling mechanisms, i.e., electron cooling, and/or introducing new pumps. Both modifications are currently under way.

During the course of this work, a lot of insight about the particulars of Doppler

cooling in the 7 T magnetic field was obtained. Specifically, the polarizations required for each of the two schemes, radial and axial, were deduced, and the corresponding laser frequencies were calculated. The laser beams had to be combined outside and inside the vacuum, and this was done also within this work. The six 854 nm frequencies needed, due to the J-mixing, are obtained from two lasers passed through an EOM driven in the microwave regime. All the lasers are stabilized [44] and meet the requirements for Doppler cooling. The optical system to collect the fluorescence photons was also designed and built. The optical path inside vacuum is about 1.5 m, and it was possible to obtain a picture of the trap region when introducing laser light through the fibers. It was confirmed that the size of the image is consistent with the trap size and the knowledge of the optical system. This is very important, as experience shows that an optical system performing adequately is essential to carry out Doppler cooling experiments.

The next step will be obtaining a fluorescence signal in the magnetic field. For this, we are improving the vacuum conditions, which is a very slow process. At the end and since everything will be detected through the axial motion, a proof of principle of the proposed measurement method has been shown from measurements obtained with an open-ring Paul trap, where single ion sensitivity was reached in 2015 [35]. The expected improvement in sensitivity is clearly shown by applying a resonant dipole field and can be directly projected to the Penning trap, since the axial motion is independent of the magnetic field. As described and already implemented, the situation in the Penning trap will require 12 frequencies, due to the non-degeneracy of the levels involved in the process, and specific polarizations.

Bibliography

[1] J. I. Cirac and P. Zoller, "Quantun Computations with Cold Trapped Ions", *Phys. Rev. Lett* **74** 4091-4094 (1995)

[2] R. Blatt and C.F. Roos, "Quantum Simulations with Trapped Ions", *Nature Physics* **8** 277-284 (2012)

[3] B.P. Lanyon *et al*, "Universal Digital Quantum Simulation with Trapped Ions", *Science* **334** 57-61 (2011)

[4] G. Werth, "Fundamental particle properties using particle traps", *J. Phys. G* **20** 1865-1883 (1994)

[5] S. Sturm, G. Werth and K. Blaum, "Electron g-factor determinations in Penning traps", *Ann. Phys. (Berlin)* **525** 620–635 (2013)

[6] E.G. Myers, "The most precise atomic mass measurements in Penning traps", *Int. J. Mass Spectrom.* **349-350** 107-122 (2013)

[7] S. Sturm *et al*, "High-precision measurement of the atomic mass of the electron", *Nature* **506** 467-470 (2014)

[8] M. Block *et al*, "Direct mass measurements above uranium bridge the gap to the island of stability" *Nature* **463** 785 (2010)

[9] D. Rodríguez *et al*, "Mass Measurement on the rp-Process Waiting Point ^{72}Kr" *Phys. Rev. Lett.* **93** 161104 (2004)

[10] A. Kellerbauer *et al*, "Direct Mass Measurements on the Superallowed Emitter ^{74}Rb and Its Daughter ^{74}Kr: Isospin-Symmetry-Breaking Correction for Standard-Model Tests" *Phys. Rev. Lett.* **93** 072502 (2004)

[11] S.Rainville *et al*, "A direct test of $E = mc^2$" *Nature* **438** 1096 (2005)

[12] M.P. Bradley *et al*, "Penning Trap Measurements of the Masses of ^{133}Cs, ^{87,85}Rb, and ^{23}Na with Uncertainties ≤ 0.2 ppb, *Phys. Rev. Lett* **83** 4510-4513 (1999)

[13] M. König *et al*, "Quadrupole excitation of stored ion motion at the true cyclotron frequency", *Int. J. Mass Spectrom. Ion Processes* **142** 95-116 (1995)

[14] E. Minaya Ramirez *et al*, "Direct mapping of nuclear shell effects in the heaviest elements", *Science* **337** 1207 (2012)

[15] G. Eitel *et al*, "Position-sensitive ion detection in precision Penning trap mass spectrometry", *Nucl. Instrum. Methods A* **606** 475-483 (2009)

[16] S. Eliseev *et al*, "Phase-Imaging Ion-Cyclotron-Resonance Measurements for Short-Lived Nuclides", *Phys. Rev. Lett* **110** 082501 (2013)

[17] R.S. Van Dyck Jr., D.B. Pinegar, S. Van Liew and S.L. Zafonte, "The UW-PTMS: Systematic studies, measurement progress, and future improvements", *Int. J. Mass Spectrom.* **251** 231-242 (2006)

[18] D. Rodríguez, "A quantum sensor for high-performance mass spectrometry", *Appl. Phys. B* **107** 1031-1042 (2012)

[19] D.J. Heinzen y D.J. Wineland, "Quantum-limited cooling and detection of radio-frequency oscillations by laser-cooled ions" *Phys. Rev. A* **42** 2977 (1990)

[20] G. Savard *et al*, "A new cooling technique for heavy ions in a Penning trap", *Phys. Lett. A* **158** 247 (1991)

[21] J.M. Cornejo, "The Preparation Penning Trap and recent developments on high-performance ion detection for the project TRAPSENSOR", PhD Thesis (2016)

[22] J.M. Cornejo and D. Rodríguez, "A preparation Penning trap for the TRAPSENSOR project with prospects for MATS at FAIR", *Nucl. Instr. Meth. Phys. Res. B* **376** 288-291 (2016)

[23] L. S. Brown and G. Gabrielse, "Precision spectroscopy of a charged particle in an imperfect Penning trap", *Phys. Rev. A* **25** 2423-2425 (1982)

[24] T.W. Hänsch and A.L. Schawlow, "Cooling of gases by laser radiation", *Optics Communications* **13** 68-69 (1974)

[25] D.J. Wineland and H. Dehmelt, "Proposed $10^{14}\triangle\nu < \nu$ Laser Fluorescence Spectroscopy on Tl+ Mono-ion Oscillator III" *Bulletin of the American Physical Society* **20** 637 (1975)

[26] W. Neuhauser, M. Hohenstatt, P. Toschek and H. Dehmelt, "Optical-Sideband Cooling of Visible Atom Cloud Confined in Parabolic Well", *Phys. Rev. Lett.* **41** 233 (1978)

[27] D.J. Wineland, R.E. Drullinger and F.L. Walls, "Radiation-Pressure Cooling of Bound Resonant Absorbers", *Phys. Rev. Lett.* **40**(25) 1639 (1978)

[28] D. Leibfried, R. Blatt, C. Monroe and D. Wineland, "Quantum dynamics of single trapped ions" *Rev. Mod. Phys.* **75** 281 (2003)

[29] S. Donnellan, "Towards Sideband Cooling of a Single $^{40}Ca^{+}$ Ion in a Penning Trap", PhD. Thesis (2011)

[30] D.R. Crick, S. Donnellan, D.M. Segal, and R.C. Thompson, "Magnetically induced electron shelving in a trapped Ca^{+} ion", *Phys. Rev. A* **81** 052503 (2010)

[31] S. Mavadia. "Motional Sideband Spectra and Coulomb Crystals in a Penning Trap", PhD Thesis (2013)

[32] B.H. Bransden and C.J. Joachain, "Physics of Atoms and Molecules", New York, John Wiley and Sons, 1983

[33] M. Colombano, "Implementación y puesta a punto de un modulador electro-óptico y mejora de las prestaciones del sistema de detección en el proyecto TRAPSENSOR", Master Thesis (2015)

[34] D. Rodríguez *et al*, "The LPCTrap facility: A novel transparent Paul trap for high-precision experiments", *Nucl. Instr. Meth. Phys. Res. A* **565** 876-889 (2006)

[35] J. M. Cornejo *et al*, "Extending the applicability of an open-ring trap to perform experiments with a single laser-cooled ion", *Rev. Sci. Instrum.* **86** 103104 (2015)

[36] J. M. Cornejo *et al*, "Optimized geometry for a Penning-(micro)-trap mass spectrometer based on connecting ions", in preparation

[37] Product web page: http://www.toptica.com/products/research_grade_diode_lasers/tunable_diode_lasers/the_ultimate_tunable_diode_laser_dl_pro.html

[38] P. Escobedo, "Desarrollo de un sistema de control para láseres de diodo utilizando moduladores acústico-ópticos", Master Thesis (2014)

[39] J. Casas, "Óptica", Zaragoza, Universidad de Zaragoza (1985)

[40] The NIST Reference on Constants, Units and Uncertainty: http://physics.nist.gov/cuu/index.html

[41] Atomic Mass Data Center: https://www-nds.iaea.org/amdc/

[42] M.J. Gutiérrez, "Experimentos de precisión con un ion de $^{40}Ca^{+}$ confinado en una trampa electromagnética", Bachelor Thesis (2015)

[43] J. Martínez, Bachelor Thesis, in preparation

[44] J.M. Cornejo *et al*, "Status of the Project TRAPSENSOR: Performance of the laser-desorption ion source", *Nucl. Instr. Meth. Phys. Res. B* **317** 522-527 (2013)